Structural manifestation of partial proton ordering and defect mobility in ice I*h*

A. D Fortes

PCCP

Accepted Manuscript

Volume 18 | Number 1 | 7 January 2016 | Pages 1–636

PCCP

Physical Chemistry Chemical Physics
www.rsc.org/pccp

ISSN 1463-9076

PERSPECTIVE
Darya Radziuk and Helmuth Möhwald
Ultrasonically treated liquid interfaces for progress in cleaning and separation processes

175 YEARS

ROYAL SOCIETY OF CHEMISTRY

rsc.li/pccp

PCCP

ARTICLE

Structural manifestation of partial proton ordering and defect mobility in ice I*h*

A. D Fortes,*[a,b]

Water ice is one of the most fundamental and well-studied molecular solids, which continues to provide surprising and useful insights into its emergent complexity as ever more precise experimental techniques are applied. Using one of the highest resolution neutron powder diffraction instruments in the world, I report a small but systematic distribution in the c/a axial ratios of D_2O ice I*h* below 160 K that depends upon both the preparation method and the thermal history of the sample. The general decrease in c/a on cooling is interpreted as a consequence of short-range partial ordering in the hydrogen-atom substructure: the synthesis-dependent variation then follows from there being a spectrum of relaxation times between samples formed by slow natural freezing, samples formed by very rapid quench-freezing and samples formed with a small amount of alkali hydroxide dopant, probably due to differences in the relative abundance of orientational versus ionic point defects.

Introduction

The water molecule's simplicity belies the emergent complex behaviour of the bulk material, which occurs by virtue of an interplay between structure, dynamics and even the experimental protocol. In the crystalline phase of ice that occurs at atmospheric pressure (ice I*h*, space-group $P6_3/mmc$), the water molecules are dynamically orientationally disordered, leading to a time- and space-averaged structure – sensed by diffraction experiments – consisting of an ordered array of tetrahedrally-coordinated oxygen atoms with two half-occupied hydrogen sites along the four vectors connecting any particular oxygen atom to its nearest neighbour;[1-3] since the hydrogen atom substructure exhibits no long-range order, it may be useful to think of it as a 'proton fluid' with a viscosity that is proportional to the relaxation time and the ability to form either a glassy solid when super-cooled, in which the disorder and its associated configurational entropy is frozen-in, or a crystalline solid that imbues the overall structure of the ice crystal with an orientationally-ordered configuration when suitably annealed.[4] In the case of ice I*h*, the viscosity (relaxation time) of the proton fluid is sufficiently high (long) at the temperature where its

'crystallization' should occur, around 70 K, that the ordered state is not seen in pure ice in the laboratory – although it may occur on geological time-scales in the outer solar system.[5] However, doping ice with a $10^{-2}–10^{-3}$ molar concentration of alkali hydroxide reduces the relaxation time by a factor of 10^9, leading to 'crystallization' of the proton fluid and the nucleation of an orientationally-ordered ferroelectric crystal known as ice XI (space-group $Cmc2_1$) in approx. 12 hr.[6-12]

The ability of molecules to re-orient themselves and/or for protons to diffuse from one site to another is necessary axiomatically (aside from the smaller probability of tunnelling) to achieve a fully ordered configuration. It remains open to question whether, in the region where such mobility occurs, a tendency towards short-range partial order of the proton fluid occurs. A variety of studies provide both experimental and computational evidence for partial ordering of ice I*h* far above the transition to ice XI. Calorimetry[13-16] reveals a fractional decrease in the configurational entropy on cooling that – in a geometrically-constrained system – can only be the result of partial ordering.[17] Likewise, measurements of the librational peak widths in FTIR studies of ice, and changes in the structure of the librational bands from inelastic neutron spectra both suggest the onset of proton ordering, certainly below 150 K and perhaps as high as 237 K.[18,19] Evidence that ice XI grows more readily from ice I*h* that has formed by back-transformation of a preceding generation of ice XI has been interpreted as being due to 'nanodomains' of short-range order persisting some tens of Kelvin above the ice XI → ice I*h* transition.[20] Finally, a recent determination of the dielectric properties of ice

a. *ISIS Neutron & Muon Spallation Source, Rutherford Appleton Laboratory, Harwell Science and Innovation Campus, Chilton, Oxfordshire, OX11 0QX, United Kingdom.*
b. *Department of Earth Sciences, University College London, Gower Street, London WC1E 6BT, United Kingdom.*
* Corresponding author email: dominic.fortes@stfc.ac.uk
Electronic Supplementary Information (ESI) available. See DOI: 10.1039/x0xx00000x

This journal is © The Royal Society of Chemistry 2019

Phys. Chem. Chem. Phys., 2019, **00**, 1-3 | **1**

ARTICLE

PCCP

through the ice XI → ice Ih and ice Ih → ice XI transitions shows an extended anomaly in the real and complex parts of the dielectric constant, attributed to an ongoing process of disordering up to ~ 125 K.[21]

It has hitherto been assumed that no such signature of partial ordering was manifested in the time- and space-averaged structure sampled by powder or single-crystal diffraction studies, although there were assorted reports of 'anomalies' in the lattice parameters or some other quantity at various temperatures; as discussed in my previous work,[22] many of these were either below the level of statistical relevance or else transpired to be irreproducible. However, a recent very-high-precision dilatometry study[23,24] reported a reproducible anomaly in the linear thermal expansion near 100 K, principally along the c-axis, in both H_2O and D_2O ice Ih, which was interpreted as a direct signature of the glass transition, the sharp rise of the thermal expansion being attributed to the propagation of lattice solitons. In terms of the linear-expansion anomaly and the overall temperature dependence of the axial ratio, c/a, the dilatometry differed substantially from the neutron powder diffraction observations that I published in 2018.[22] Amongst other inaccurate comments about my work, Buckingham et al.[24] wrongly attributed these differences to a general deficiency of the powder diffraction method; the anomalies that they communicated were detectable by me but unambiguously were not detected in my high-precision D_2O measurements. *This is not a flaw, it is a clue*. Indeed, high-resolution powder diffraction is potentially a powerful probe of this problem, since it is able to make absolute measurements of lattice parameters and to characterize samples produced by more diverse methods. In systematically evaluating the role of sample synthesis and thermal history here, we will discover that powder diffraction can bridge the realms of dilatometry, calorimetry and dielectric spectroscopy, providing a valuable insight into the underlying dynamical processes.

In addition to the three separate D_2O ice Ih samples described previously,[22] I prepared a further four D_2O samples and subjected these to seven distinct thermal protocols, collecting high-resolution neutron powder diffraction data at temperatures between 1.5 and 270 K. Taken together, the fourteen warming/cooling curves allow us to discern the interaction between structure and dynamics in ice and suggest avenues for further work.

Experimental methods

Liquid D_2O (99.96 atom % D, Sigma 151890) was decanted into polyethylene tubes that had previously been soaked in 99.9 % D_2O. The tubes were sealed and placed in a freezer at 256 K, where the contents froze naturally to a clear and largely bubble-free solid. Lumps of this ice were extracted and ground to a fine powder under liquid nitrogen. The powder was then transferred into a nitrogen-cooled slab-geometry Al-alloy (6082-T6) sample holder of the same kind used in my previous study (sample geometry 18 x 23 mm perpendicular to the beam, and 15 mm depth parallel to the incident beam).

Flash-frozen ices were prepared by (1) pouring liquid D_2O directly into liquid nitrogen, and (2) by immersion of small pipette droplets directly into liquid nitrogen. These solids were ground and loaded into slab-geometry sample containers in the same manners as the naturally frozen ice described above.

A sample of doped ice was prepared by addition of 2mM of KOD (40 wt % in D_2O, 98 atom % D, Sigma 176761) to D_2O (99.96 atom % D, Sigma 151890). This liquid was pipetted into liquid nitrogen, ground to a fine powder and loaded into the pre-cooled Al-alloy slab-geometry sample holder. The entire process, from addition of KOD to D_2O through to loading of the sample holder was done under an inert helium atmosphere in order to avoid 'deactivation' of the KOD by reaction with atmospheric CO_2.

Time-of-flight neutron powder diffraction data were collected using the High Resolution Powder Diffractometer (HRPD) at the ISIS Neutron & Muon Spallation Source, Rutherford Appleton Laboratory, UK.[25] The data collection was done in a neutron time-of-flight (TOF) 'window' between 30 and 130 milliseconds in the instruments' three detector banks. All of the high-precision lattice parameter refinements were obtained from the highest resolution backscattering detector banks (average 2θ = 168.33°) where the measured TOF range corresponds to d-spacings between 0.65 and 2.65 Å. Some data from the banks at 2θ = 90° were used to evaluate the samples for stacking defects and other evidence of microstructure since these detectors observe d-spacings out to 4.0 Å (in this TOF window) where the strongest Bragg peaks from D_2O ice Ih occur.

Low temperatures were produced by means of a closed-cycle refrigerator (CCR), equipped with a Sumitomo Heavy Industries Ltd., RDK-415D2 cryo-cooler, mounted in the instrument's sample tank. The normal protocol was to maintain the temperature of the CCR cold head 30 – 40 K below the sample temperature whilst using a Watlow Firerod C1E-192 cartridge heater inserted in the sample holder itself to actively heat and control the sample temperature. The sample temperature was measured using a RhFe resistance thermometer (fully-calibrated to ITS-1990), also inserted into the body of the sample holder. A number of different measurement protocols were applied to this sample but the common feature throughout was the application of care to ensure excellent thermal equilibration of the sample, over and above the standard used in the previous experiment. Thus, all warming / cooling ramps (unless otherwise stated) were no larger than 3 K min^{-1} and the thermal equilibration prior to every measurement involved a wait of 10 minutes once the sample temperature was within 0.5 K of the requested set point. Measurements on the KOD-doped ice were carried out in a helium-flow cryostat but the protocol for controlling and ramping of the sample temperatures was identical to that used for the pure ice loaded in the CCR.

All data underwent initial processing using the *Mantid* suite of powder-diffraction routines, focusing data in each detector bank to a common scattering angle and then using a V:Nb null-scattering standard material to normalize with respect to the spectrum of the incident beam and correct for instrumental efficiency.[26] The output data, in the form of logarithmically-binned histograms, were then analyzed by the Rietveld[27] and LeBail[28] whole-pattern fitting methods using *GSAS/Expgui*.[29,30]

A summary of the different samples and thermal protocols is provided in Table 1 and a more thorough description is given in the ESI. The refined lattice parameters, derived c/a ratios and the derived linear and volume thermal expansion coefficients are tabulated in the Supplementary Material, Data Tables S1 and S2.

2 | *Phys. Chem. Chem. Phys*., 2019, **00**, 1-3

This journal is © The Royal Society of Chemistry 2019

Table 1 Summary of the measurement series referred to in this work.

Series 1	Naturally-frozen D_2O ice Ih, slowly cooled / slowly warmed.
Series 2	Naturally-frozen D_2O ice, quenched at 170 K /min from 265 K and slowly warmed.
Series 3	Naturally frozen D_2O ice, cooled at 15 K /min from 170 K and then slowly warmed.
Series 4	Flash frozen globule of D_2O ice measured on slow warming.
Series 5	Flash frozen pipette droplets of D_2O ice measured on slow warming.
Series 6	Flash frozen KOD-doped D_2O ice with long anneal at 70 K
Series 7	Flash frozen KOD-doped D_2O ice, slowly cooled / slowly warmed.

As in the previous study, it is necessary to demonstrate that the sample preparation – particularly of the flash-frozen specimens – does not result in the presence of substantial stacking defects. Indeed the calculations of Malkin et al.[31] suggest that even naturally-frozen ice is subject to a certain proportion of stacking faults. Stacking faults produce quite characteristic effects on the diffraction pattern, seen most sensitively in the width of the (002) Bragg peak and in the diffuse scattering around that peak (see Supplementary Fig. S7). As shown in Supplementary figures S5 – S6, neither the naturally-frozen nor the flash frozen ices samples used in this work exhibited any evidence that would be considered diagnostic of stacking faults.

There are significant systematic differences in the widths of all peaks, not just (002), between the naturally-frozen and the flash-frozen samples, a difference that varies with temperature. In Figure S6, the FWHM of both the (011) and (002) peaks are as much as 8 % larger in the flash-frozen samples, and this broadening diminishes on heating above 150 K to match the peak widths of the slowly-frozen ices. It is worth noting three things: firstly, the magnitude of the broadening is not systematic, being comparatively small in the flash-frozen samples from the earlier study, probably reflecting other aspects of the sample preparation such as the amount of grinding done and the degree of care devoted to keeping the ice absolutely at liquid nitrogen temperatures; secondly, the peak widths exhibit no features in common with the axial ratio plots (*cf*., Figure 1), indicating that the process responsible for the discontinuities in the 110 – 130 K range have no direct relationship; thirdly, the naturally-frozen ice that was quenched from 265 – 77 K in 90 seconds shows no sign of strain broadening so the broadening is attributable to the sample preparation rather than the subsequent thermal protocol (Figure S6c, S6d). Rietveld analysis of the powder data at base temperature indicates that the additional broadening is a particle-size effect rather than being due to inhomogeneous strain; the model domain size at 10 K is 0.8 μm for the flash-frozen droplets and 2.3 μm for the naturally-frozen ice. A primary extinction parameter, which is required to fit the intensities of the strongest Bragg peaks, also exhibits a larger value in the naturally-frozen ice (210 μm^2) than in the flash-frozen ice (60 μm^2), consistent with a smaller domain size in the latter.

Results

The temperature dependence of the axial ratio, *c/a*, in ice I*h*

Figure 1 shows the temperature dependence of the *c/a* ratio found in my previous work[22] on flash-frozen D_2O droplets compared with the axial ratios obtained in the current study. In naturally-frozen slow-cooled ice the *c/a* ratio rises initially as the temperature falls, peaking at around 200 K, before dropping to a minimum near 100 K; this sigmoidal curve closely resembles the one obtained from dilatometry[23,24] for both H_2O and D_2O ice I*h*. There is no discernible hysteresis between the measurements made on slow cooling and slow warming and the *c/a* ratios above 150 K are in close agreement (within 10 ppm) with those found in my earlier work and all of the subsequent measurement. When ice that had been warmed slowly to 265 K was then quenched by immersion in liquid nitrogen and thereafter cooled more slowly from 77 to 10 K (point 1 in Fig. 1b and 1c), the sample retained the high-temperature axial ratio even though the lattice parameters themselves were reduced; on warming, however, the axial ratio displayed a step change between 100 – 110 K from what appears to be a frozen-in high-temperature state onto the same sigmoidal curve observed in the slow-cooled samples. The *c/a* ratio followed this curve on further warming and on subsequent re-cooling back down to 10 K. This behaviour is reminiscent of the anomalous variation of C_{60} fullerene's lattice-constant on approach to the glass-transition, T_g, where large differences between heating and cooling rates lead to the system unquenching on warming at a lower T than the system quenched upon cooling.[32] Efforts were undertaken to implement the model used by David et al.[32] to determine relaxation times and activation energies in these ice samples from the time dependence of the approach to equilibrium; however, the magnitude of the effect relative to the uncertainties and the available number of useful points are too small. In this respect, dilatometry would be the superior choice of method.

An attempt was made to try and freeze-in a higher value of the axial ratio by warming the sample to 170 K and then cooling it as fast as possible (in practice about 15 K min^{-1}) to point 2 on Figure 1d. Like the first quenched sample, this preserved a slightly higher *c/a* ratio that dropped sharply at ~ 110 K to merge with the slow-cool/warm sigmoidal curve.

Similar tests were then done with ice prepared by flash freezing. Rapid freezing of large quantities of D_2O (several cm^3) at one time yielded similar results to the naturally-frozen and then quench-cooled samples; the *c/a* ratio was elevated at base temperature and then merged with the sigmoidal curve after a discontinuity (Figure 1e). The main difference with the naturally-frozen ice is that the discontinuity is no longer sharp; instead of dropping immediately onto the sigmoidal curve at 100 – 110 K, the *c/a* ratio falls slightly and then follows a shallower curve until it merges with the sigmoid
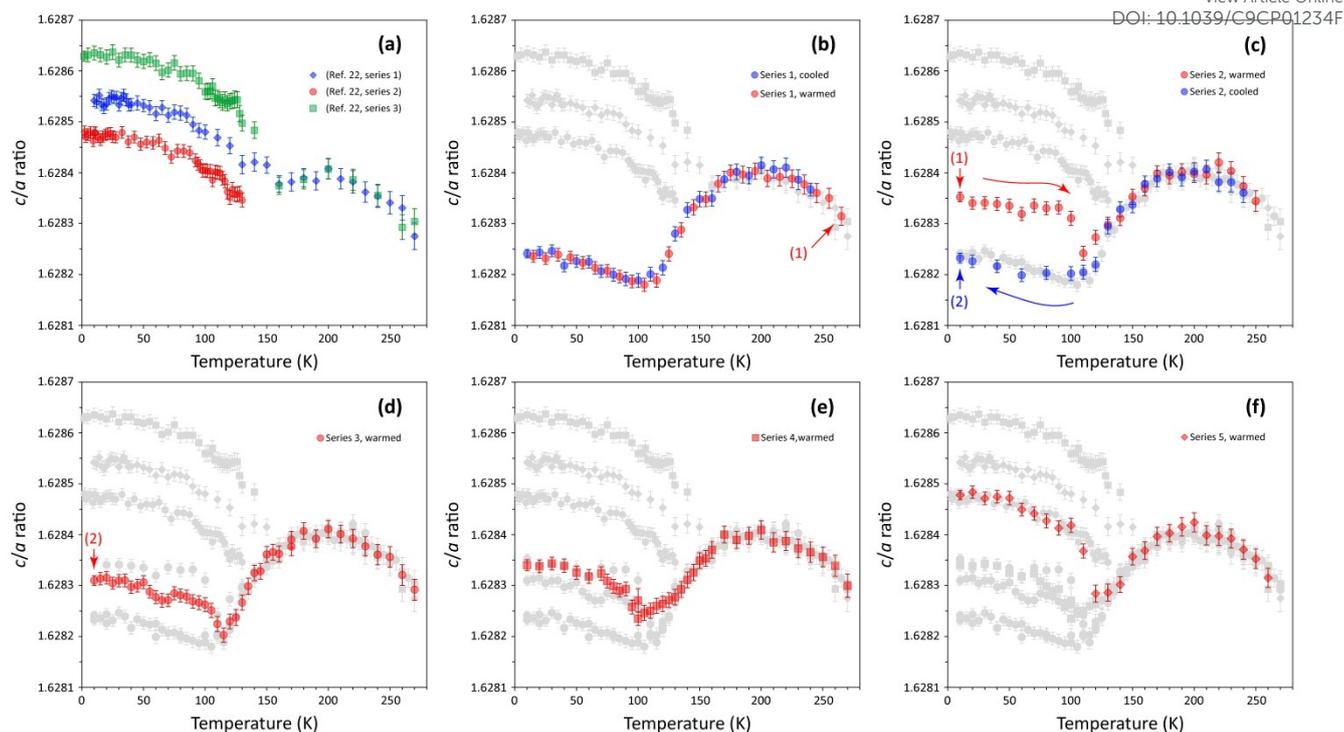
Fig. 1. Summary of c/a axial ratios measured in all pure D_2O ice samples. In each successive panel, the values shown in the preceding panels are shown in grey to provide quantitative context: **(a)** values obtained for the three quenched D_2O samples reported previously;[22] **(b)** results of this work Series 1; **(c)** this work Series 2; **(d)** this work Series 3; **(e)** this work Series 4; **(f)** this work Series 5.

at approximately 130 K. Rapid freezing of mm-sized pipette droplets yielded results in line with my earlier study,[22] trapping a substantially higher c/a ratio at base temperature (Figure 1f). The c/a ratio exhibits a fall at ~ 110 K though not enough to drop directly onto the sigmoidal curve; the temperature sampling was coarser for this specimen but the observations suggest that only about half of the expected change in the c/a ratio occurred with the point at 120 K recreating a similar behaviour to Figure 1e in the range 110 – 130 K.

On slow cooling and slow warming the c/a ratio of KOD-doped ice closely follows the sigmoidal curve of pure ice Ih above 100 K (Fig. 2a). However, the decrease of c/a continues below 100 K, indeed it steepens as the curve extends to ~ 60 K; the minimum value of c/a is thus much smaller than is observed in pure ice Ih (Figure 2b). Furthermore, annealing at 65 – 70 K leads to an additional time-dependent relaxation of the lattice parameters and ultimately to the appearance of Bragg peaks forbidden by the space-group symmetry of ice Ih and associated with the nucleation of ice XI. Doping with ~2 mM KOD has a result that is almost indistinguishable from that observed previously in 80 mM KOD-doped ice Ih after back-transformation from ice XI.[9]

Overall, these results show that the c/a ratio of many different samples of D_2O ice above 150 K is the same (to within about 10 ppm) regardless of how the ice was crystallized, what thermal treatment it was subjected to and even the level of ionic doping. Below 150 K, a comparatively large variation (250 ppm) of the axial

ratio is observed in pure ice, with smaller values occurring in samples of naturally frozen ice with larger diffracting domains; larger c/a values occur in samples of flash-frozen ice with smaller diffracting domains. Departures from these upper and lower limits in c/a ratio then seem to depend on the thermal history of the ice after crystallization. The greatest contribution to the difference in c/a ratios between the flash-frozen and the naturally-frozen ices is the length of the crystal's c-axis – notably, the direction along which the crystal becomes polarized when the proton substructure is fully ordered.[6,7,9]

No new measurements were made on H_2O ice Ih additional to those reported previously, since the large incoherent neutron scattering length of ordinary hydrogen imposes substantial constraints on the number and quality of observations one can obtain, compared with deuterated material. However, comparison of the older quench-frozen H_2O droplet's c/a ratios[22] with the entire set of pure D_2O values (Figure 3) reveals informative similarities. The 'equilibrium' sigmoidal curve is present (if not as precisely defined) as well as a sharp relaxational dip at ~ 110 K. It is worth remarking on the fact that the onset of the relaxation occurs at approximately the same temperature in H_2O and D_2O. This differs from the dilatometric observations, where an isotope effect of ~ 25 K is reported.[23,24] The origin of the disagreement is actually in the D_2O results where the relaxation I observe occurs quite reproducibly in the range of 100 – 110 K and not at 125 K.

PCCP
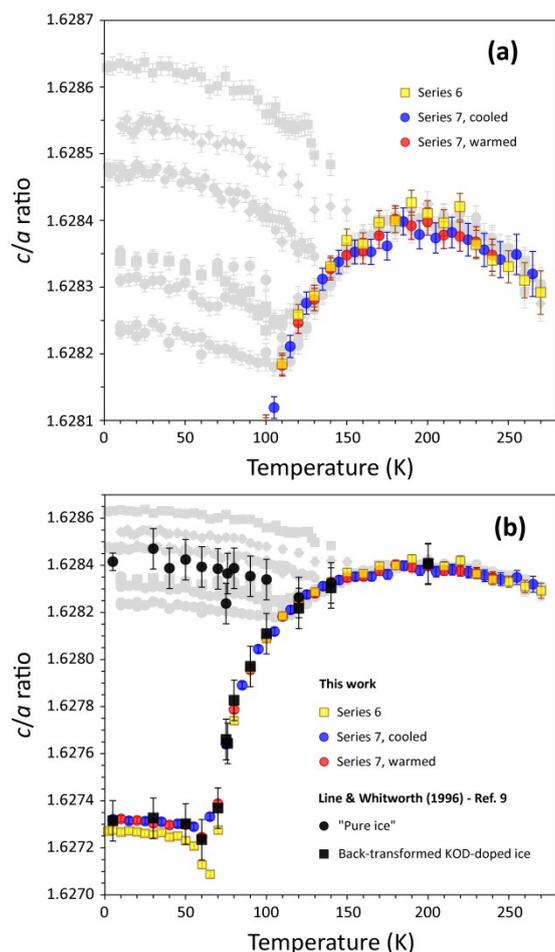
Fig. 2. Summary of c/a axial ratios measured in KOD-doped ice samples (Series 6 and 7), shown on the same vertical scale as the pure D_2O results **(a)** and in their wider context in **(b)**.
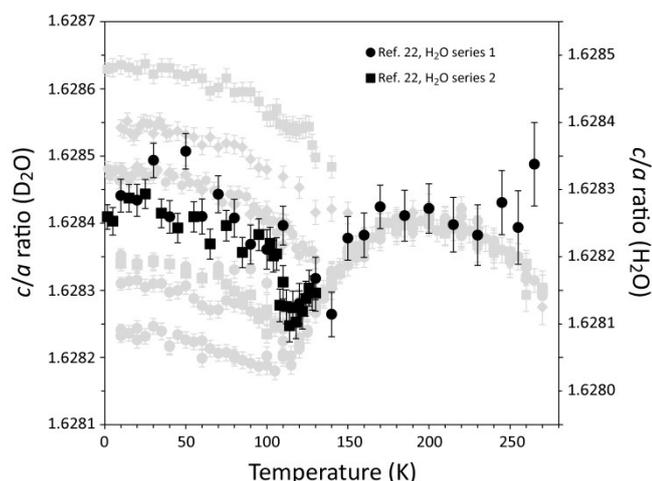

Fig. 3. The earlier results[22] for H_2O are plotted on an expanded scale and overlaid with the new D_2O data (grey symbols). Note that the right-hand scale for H_2O ice is offset vertically (but not stretched) in order to afford a good visual comparison.

Thermal expansion anomalies in ice Ih

Although the distribution in the absolute length of the c-axis below 100 K is quite large (almost 3 % of the total variation on warming from 0 – 270 K) and nearly five times larger than the absolute variation of the a-axis length at low temperature, the signature of this in the linear thermal expansion remains small. Fig. 4a and 4b shows the linear expansion of the crystallographic axes, α_a and α_c, determined from the slowly-cooled and slowly-warmed naturally-frozen ice, compared with one of the flash-frozen specimens reported previously[22] in which there was only a quite broad and shallow variation in c/a between 100 and 150 K. In the data from the naturally-frozen ice between 100 and 150 K there is an excess in α_c – leading to a clear 'knee' in the linear expansion at 120 K; there is no significant anomaly in the linear expansion along a. By contrast, Fig. 4c and 4d make the comparison with the sample prepared by flash-freezing of pipette droplets, in which the frozen-in c/a ratio exhibits a fairly abrupt decrease on warming to ~ 110 K. Now, one observes a plateau in α_c followed by a steep rise and, again, no equivalent anomaly in α_a. The latter type of expansion anomaly most closely resembles those reported for H_2O and D_2O ice Ih by Buckingham et al.,[23,24] the position and depth of which were stated to depend on the cooling history of the sample. The dilatometry study[23,24] appears to have characterized only one sample of D_2O ice so it is not possible to say much about systematic differences or reproducibility.

The very steep upturn of c/a at 70 K in KOD-doped ice produces a sharp thermal expansion anomaly along both a and c (Figure 4e and 4f). The linear expansion of the a-axis turns negative during the anomaly whilst α_c spikes to a large positive value comparable with the expansion measured at much higher temperatures before dropping to a plateau and then resuming its 'normal' behaviour.

The volume thermal expansion, α_V, apart from small variations between 100 and 130 K, does not differ significantly between any of the pure-ice datasets measured in this work (Figure S1a) or those measured previously (Figure S1b). As described in ESI section S3, re-evaluation of the double-Debye + Einstein model fitted before gives parameters that are little different. The fit residuals demonstrate that there is noticeable disagreement only at temperatures close to the melting point; otherwise all of the volume thermal expansion determinations for pure ice are highly reproducible and significantly different from the Buckingham group's single D_2O dataset. The dilatometry values of α_V agree very well with the diffraction values below 60 K but exhibit a growing deviation that accelerates above 225 K. The acceleration seems likely to reflect an incomplete correction for sublimation, which I note was corrected in their D_2O sample using calibration measurements done on H_2O ice samples (Supplement of Ref. 24).

Between ~ 60 and 100 K in KOD-doped ice Ih there is a large positive deviation of α_V away from the Debye-Einstein model used for pure D_2O ice Ih (Figure S1c). Otherwise, the thermal expansion of KOD-doped ice exhibits the same features as pure D_2O ice Ih, a negative expansion region of the same depth and location at low-T and a slight positive deviation from the model at high-T.

In order to obtain a clearer picture of the type of anomalies one would expect to see in the linear expansion for particular c/a temperature dependences, and as a potential aide to interpreting

This journal is © The Royal Society of Chemistry 2019

Phys. Chem. Chem. Phys., 2019, **00**, 1-3 | **5**

the dilatometry measurements, I have derived an analytical approximation to $c/a(T)$ and the temperature dependence of the a-axis, as described in detail in ESI Section S4. A set of example models are shown in Figure 5: parts (a) – (c) depict a series of frozen-in axial ratios at low temperature that undergo broad and shallow dips between 100 – 150 K, merging smoothly with the higher-temperature sigmoidal curve; parts (d) – (f) depict frozen-in axial ratios where comparatively sharp relaxations occur before joining the sigmoidal curve. It is clear that the red and black lines in parts (a) – (b) correspond with "Series 1" in Fig 1a and "Series 1" in Fig. 1b, respectively, and the c-axis expansion behaviour shown in Figure 4b. The orange dashed line in parts (d) – (f) is a reasonable approximation to the $c/a(T)$ behaviour shown in Figure 1f and the linear expansion anomaly in Figure 4d. Other possible $c/a(T)$ behaviours, including those resembling the observations from KOD-doped ice, are modelled in the Supplementary Information (Figures S2 – S3).

What these models confirm is that the magnitude of expansion anomalies such as those seen by Buckingham et al.[23,24] depends on the derivative of c/a with respect to T and only occur when there is a substantial structural relaxation of the c/a ratio from a frozen-in high-temperature value to the 'equilibrium' sigmoidal curve; when ice is cooled and warmed sufficiently slowly, no such anomaly occurs. In other words, the Buckingham group's thermal expansion anomaly only occurs when the proton 'glass' unquenches at a lower temperature on warming than it became quenched on cooling. It is therefore not directly a signature of T_g, but of a substantial mis-match between cooling and warming rates in the vicinity of T_g. Ice can be slowly cooled and warmed through T_g without producing any anomaly in the thermal expansion. This is by no means a statement that the conclusion reached by Buckingham et al.[24] is incorrect, simply that their observations do not reflect the full scope of the thermal expansion behaviour in ice.

Discussion

The observations detailed above can be understood in terms of the interaction between three different aspects of the ice crystal. First, there is an intrinsic degree of elastic isotropy to the ice framework whereby, when no structural changes occur, the c/a ratio is almost independent of temperature, rising slightly on cooling and saturating below ~ 50 K. Secondly, there is some characteristic of the structure that begins to change below ~ 200 K, resulting in a greater shortening of the c-axis on cooling than the a-axis and a steepening drop of the c/a ratio. Thirdly, there is an aspect of the
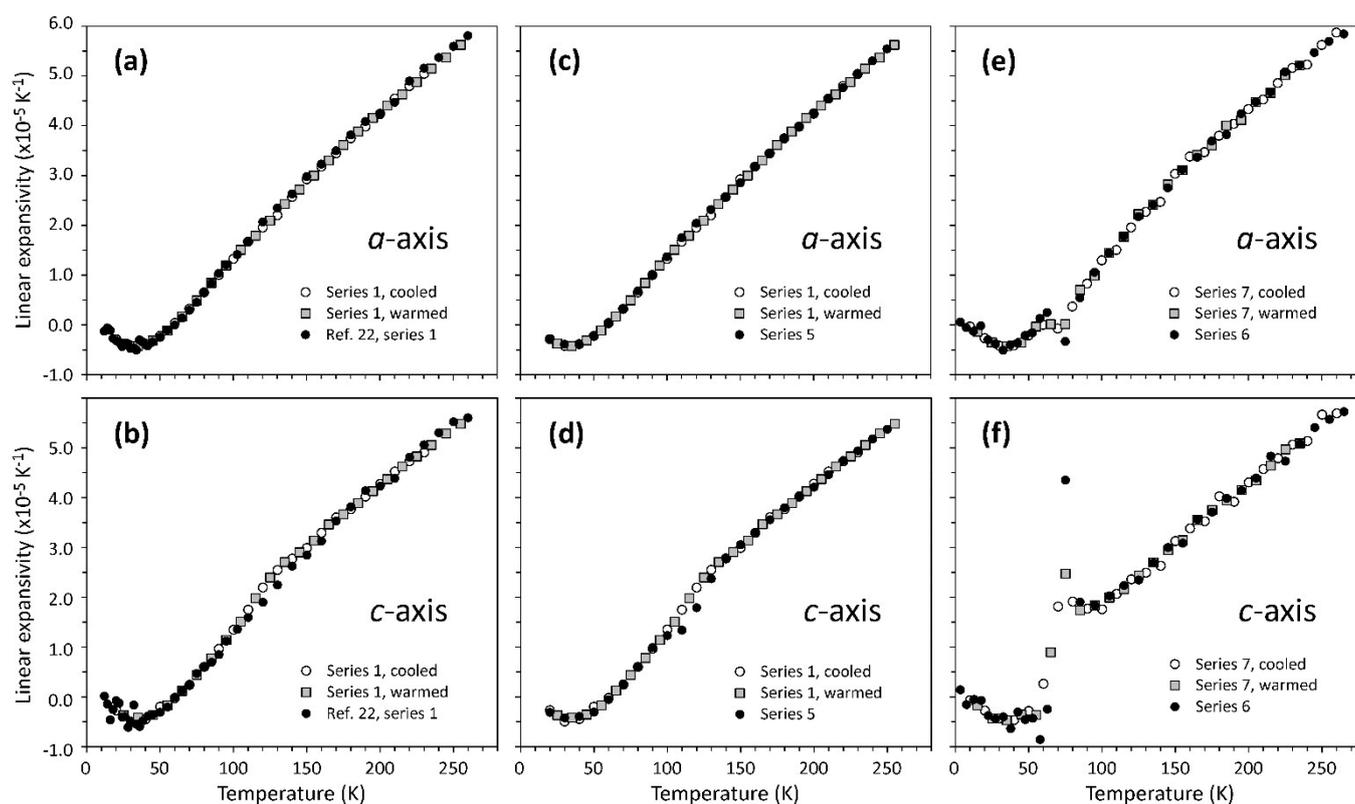
Fig. 4. Linear thermal expansion coefficients of D_2O ice. Adjacent pairs of lattice parameters are used to derive unit-strain tensors as a function of temperature, from which the linear expansivities (symbols) are derived. Error bars are omitted for clarity although the degree of scatter is a good indication of the small systematic error. Parts **(a)** – **(d)** report data for pure D_2O ice; parts **(e)** and **(f)** are from KOD-doped D_2O ice.

6 | *Phys. Chem. Chem. Phys*., 2019, **00**, 1-3

This journal is © The Royal Society of Chemistry 2019

structure's behaviour that determines the rate at which the second process proceeds. Hence, the variation in c/a occurs because of a temperature-dependent but sample-independent structural change, but the fact that a distribution in c/a is seen at low temperature is due to temperature-dependent and sample-dependent dynamics.

The dynamic aspects of molecular reorientation (and concomitant defect microstructure) in ice are typically probed by dielectric spectroscopy;[33] It is well-known that a substantial distribution of relaxation times exists below ~ 230 K in pure ice Ih,[34] the origin of which has been the subject of debate. Above 230 K there is a single relaxation process with an activation-energy of ~ 58 – 59 kJ mol^{-1}, which is interpreted as being due to the relaxation of orientational defects (Bjerrum type L and type D) with a molar abundance of ~ 10^{-7}. Below 230 K, as the concentration of thermally-generated Bjerrum defects diminishes, most studies show a crossover to a relaxational process involving ionic defects (OH$^-$, H$_3$O$^+$) with an activation-energy of ~ 20 – 22 kJ mol^{-1}, often steepening again at the lowest temperatures (Suppl. Fig. S4).[35-42] The fact that some workers report a continuation of the first relaxation process to much lower temperatures, and a spectrum of behaviour between the two extremes, has been suggested recently to be the result of sample preparation[33] and a several models have

been proposed to explain the observations.[33,43-47] In general, these state that orientational defects serve as traps for ionic defects, blocking proton hops and leading to an increase in the relaxation time. Sasaki et al.[33] inferred that the growth speed of ice affected the abundance of "impurity-produced orientational defect(s)" and that this influenced the relaxation time.

It is evident from the spread of dielectric and calorimetric observations with relaxation times of 10^3–10^4 seconds (corresponding with the typical duration of a powder diffraction measurement), indicated by the shaded region on Supplementary Figure S4, that one would anticipate dynamic behaviour to become frozen in between 150 K and 100 K for pure ice samples with a high or low orientational defect abundance, respectively. Grain boundaries are, inevitably, regions of higher orientational defect density that, by the correlated nature of proton motion in ice, can exercise control over the relaxation dynamics of the grain interior.[48,49] We expect intuitively that ice formed by flash-freezing in liquid nitrogen will be finer-grained than ice formed by slow natural freezing and thus have a higher density of grain boundaries. This is borne out by the larger Bragg-peak half-widths found in the flash-frozen ices, which refinement reveals to be a particle-size effect (see Experimental Methods). I conclude that the distribution
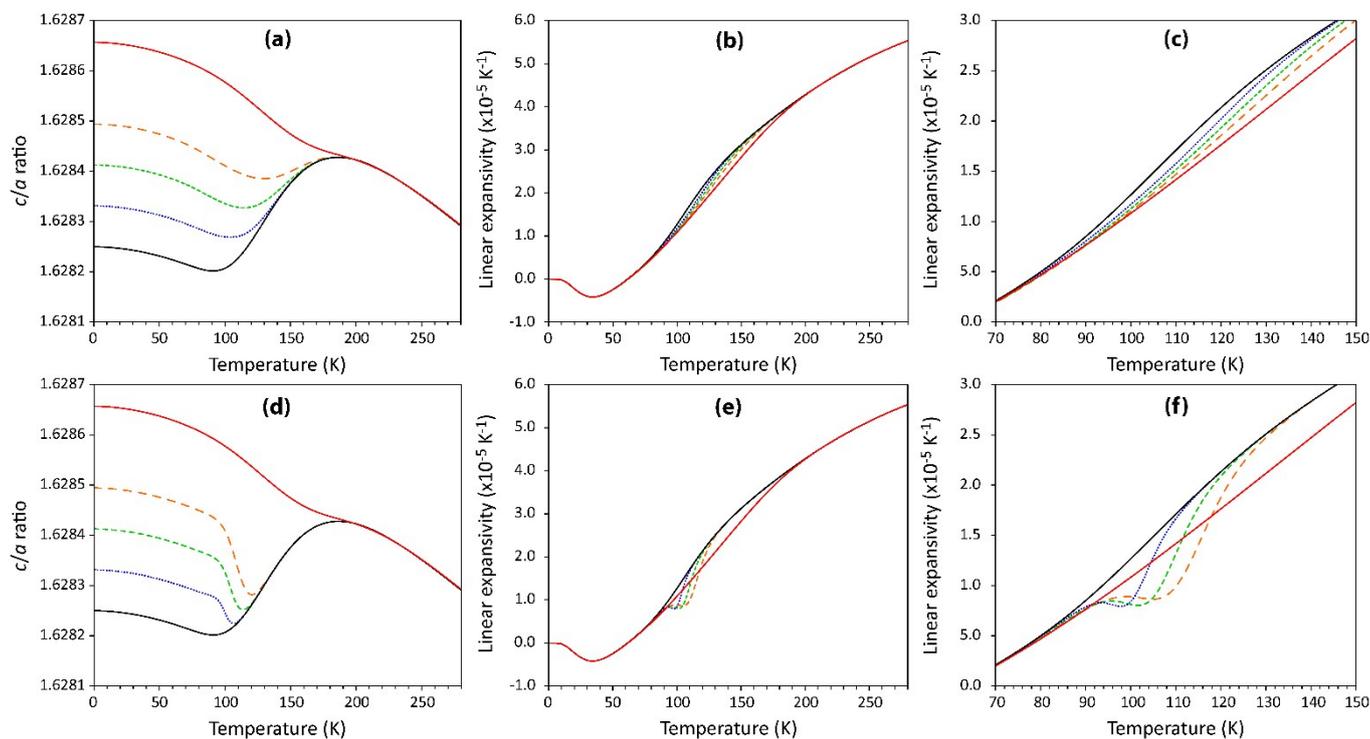
Fig. 5. Analytical models of the c/a temperature dependence. When a range of c/a values at low temperature merge smoothly with the sigmoidal equilibrium curve **(a)**, the result shown in **(b)** and magnified in **(c)**, is a small dispersion of α_c across a wide temperature range. When the same low-T c/a ratios undergo rapid change around the glass transition **(d)** then the resulting linear expansion along the c-axis [**(e)** and **(f)**]exhibits a sharp plateau-like anomaly followed by a steep rise. Compare with Figure 6.7a in Ref. 23

of temperatures over which the structurally-induced variation of *c/a* in pure ice becomes locked in is determined by the extrinsic orientational defect concentration as a result of differences in sample synthesis.

Shifting the balance in the opposite direction, adding an excess of ionic defects by doping with KOH or KOD, reduces the dielectric relaxation times by a factor of 10^9 at 100 K.[8] As a result of the persisting mobility, the *c/a* ratio continues to decrease, becoming locked in around 60 – 70 K. Annealing in the region of 65 – 70 K leads to ongoing reduction of the *c/a* ratio for as much as 12 hr prior to the appearance of symmetry-forbidden peaks indicative of the nucleation of ice XI.

Clearly, the nature and abundance of point defects in the ice crystal is the determining factor in the dynamics, controlling when and how rapidly structural elements that are manifested in the lattice parameters may change. The question remains, what are these structural changes? There are only two possible structural dimensions that may change with temperature, one being the concentration of intrinsic thermally-activated orientational defects, and the other being the degree of configurational order. It is straightforward to eliminate the first possibility. Following the example of Johari,[17] the molar concentration of L- and D-type Bjerrum defects at 200 K, corresponding with $(c/a)_{max}$, is ~ 1.5×10^{-11}, decreasing to ~ 1×10^{-25} at 110 K and ~ 1×10^{-51} at 60 K. Thus, most of the change in orientational-defect concentration occurs between 200 and 110 K, and the change on further cooling to 60 K is 14 orders of magnitude smaller. By contrast, the change in *c/a* on cooling from 110 to 60 K is more than four times larger than the change between 200 and 110 K. Similarly, examination of the various quench-cooled ice specimens shows that it is possible to freeze-in a high-temperature value of the structural parameter, which then adjusts sharply (typically a drop of *c/a*) towards the equilibrium value when warmed sufficiently for the structure to become unquenched. If we assume that it is possible to freeze-in the 270 K defect concentration, then one would expect the pure ice crystal to adopt the 110 K concentration on unquenching, a change from ~ 4×10^{-7} down to 1×10^{-25}. Firstly, it is difficult to envision how a 0.4 micromolar alteration of defect concentration could have any measureable effect on the lattice parameters and secondly there is no obvious reason why this effect should be manifested principally in the length of the *c*-axis. Again, following Johari,[17] the enthalpy change (ΔH) associated with this drop in defect concentration would be 0.026 J mol^{-1} and the entropy change (ΔS) would be 4.9×10^{-5} J mol^{-1} K^{-1}. Calorimetric determinations of the reduction in entropy during annealing around T_g are ~ 0.04 J mol^{-1} K^{-1};[13-16] hence, the most optimistic estimate of ΔS from unquenching of orientational defects is too small by almost a factor of 10^3. We should be conscious of the fact that it is much more likely for the structural parameter to become frozen in between 200 and 150 K, so the more plausible changes in concentration and thermodynamic quantities will be between 4 and 10 orders of magnitude smaller than those given above.

The second possible explanation for the temperature dependent structural changes is short-range partial ordering, which remains consistent with complete long-range disorder of the crystal.[50] The effective pseudo-hexagonal *c/a* ratio of ice XI is ~

1.6200,[9] although this value was measured in samples in which there may have been some residual partial disorder and domain-boundary strain imposed by a surrounding matrix of unaltered ice I*h*. The preference for ferroelectric ordering along *c* leads to the observed shortening of the *c*-axis in ice XI. That we observe *c/a* trending towards lower values due mainly to an excess shortening of the *c*-axis as ice is cooled, and indeed that *c/a* continues to fall as a function of time during annealing at 65 – 70 K until ice XI nucleates, is interesting circumstantial evidence for partial ordering.

The entropy change on annealing at 110 K amounts to ~ 0.7 % of the total calculated configurational entropy of ice. The relationship between ΔS and the order parameter is not linear[51] and the observed ΔS corresponds to a 7.4 % increase in the order parameter. If we consider that $(c/a)_{ord}$ = 1.6200 equates to complete order,[9] then the change in the *c/a* ratio of pure ice on cooling from 200 to 110 K represents ~ 2.4 % of the difference between a fully disordered and a fully ordered crystal. Unlike the analysis of defect abundances, these values are at least comparable orders of magnitude and it is reasonable to infer that any effect of partial ordering on the crystal is in some way diluted by the development of local strains, depending on its exact nature.

Conclusions

Figure 6 gives a schematic overview summarizing the way in which I conclude that variations in structure and dynamics affect the axial ratio of ice. The 'equilibrium curve' depicts the trend in *c/a* as ice is cooled and begins to partially order around 200 K; this curve is exceptionally well-defined by the measurements and is highly reproducible. In pure ice grown slowly such that the grains are large and there is a low abundance of surface defects, the partial ordering process freezes at ~ 100 K so that *c/a* ratios saturate in region (1). On warming through T_g (dashed near-vertical line), the proton 'glass' melts; any quenched partial order adjusts to the equilibrium curve leading to drops in *c/a* in region (2).
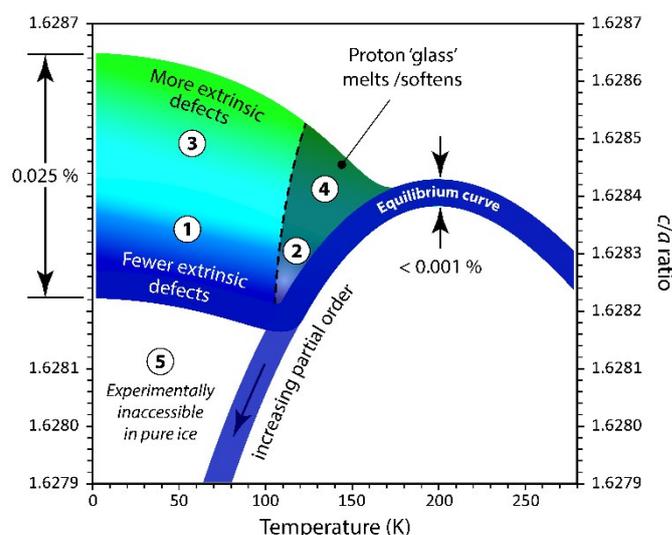

Fig. 6. Summary phase diagram of ice's dynamic behaviour.

8 | *Phys. Chem. Chem. Phys*., 2019, **00**, 1-3

This journal is © The Royal Society of Chemistry 2019

PCCP

For quench-grown ice with small grains and high surface defect abundance, the longer relaxation times lead to partial order being frozen in almost immediately at 150 – 160 K such that c/a now saturates in region (3). When such samples are warmed above T_g, the proton 'glass' melts but retains a high effective viscosity (long relaxation time) such that the quenched partial order cannot completely equilibrate in region (4), if at all. Only with addition of ionic defects (such as by doping with alkali hydroxide) does region (5) become experimentally accessible on laboratory time-scales.

Powder diffraction offers a powerful complement to the spectrum of techniques more commonly used to study dynamics in ice, such as dielectric spectroscopy, and to the very high-precision 'structural' studies of narrower scope, such as dilatometry. Powder diffraction – particularly with a bulk probe like neutron radiation – places comparatively few restrictions on sample preparation, having no special requirements for electrical or physical contact, surface planarity or crystal orientation. Indeed the measurement of quench-formed polycrystalline ice that was crucial to understanding the context of this measurement ensemble would either not be possible, or else be very difficult, using the other methods mentioned above. Whilst the precision is unquestionably poorer than the dilatometry, there can be no doubt that these powder diffraction data offer a perspective on the dynamics that is in good agreement with the literature on relaxation times in ice as well as a potential proxy for the degree of configurational order that may be much more sensitive than the calorimetric measurements. It appears that some short-range partial ordering occurs at quite high temperatures, perhaps up to 200 K, which is in agreement with some of the spectroscopic arguments advanced by Fukuzawa et al.[18,19] Although I think their work is not without flaws, it was nevertheless probably incorrect of Fortes et al.[52] to interpret Fukazawa's result as suggesting the presence of long-range proton-ordered domains in ice at these higher temperatures.

The nature of the partial ordering in ice, whether it consists of small ordered domains or perhaps a macroscopic superposition of quantum states is not clear.[53] The degree of long-range correlated behaviour of the proton fluid suggest that a (cold) plasma might be a more useful analogy than an ordinary liquid,[54] as there are both geometric constraints and long-range electrostatic interactions involved. In this case, the orientational order-disorder transition may share interesting phenomenology with the melting of plasma crystals,[55] where 'islands' of short-range-ordered material co-exist within 'streams' of disordered material, similar perhaps to the nanodomains reported in back-transformed ice.[20]

Diffuse neutron scattering from single-crystals, or total-scattering studies of polycrystals, should be able to provide direct insight into the presence and nature of partial ordering in principle; however, the signal due to static disorder occurs alongside a substantial contribution from thermal diffuse scattering and interpretations have thus far proven to be strongly model-dependent.[56-60] In temperature-dependent studies it is also not clear how quickly crystals were cooled to their measurement temperature or what heating rates were used. Furthermore, the anticipated small degrees of partial order (a few percent) make it appear unlikely that any resultant diffuse signature could be unambiguously disentangled from other sources.[61]

Conflicts of interest

There are no conflicts to declare.

Data and materials availability

The author declares that all processed numerical data required to support the conclusions of this work are provided in the Supplementary Information. The raw diffraction data and associated metadata are archived and can be provided by the author on request:

doi:10.5286/ISIS.E.95699847

doi:10.5286/ISIS.E.98018903

Acknowledgements

Notes and references

1 N. Bjerrum, Structure and properties of ice I. The position of hydrogen atoms and the zero-point entropy of ice. Kong. Dansk. Vidensk. 1951, **27**, 3–56.
2 N. Bjerrum, Structure and properties of ice. Science, 1952, **115**, 385–390.
3 S. W. Peterson, H. A. Levy, A single-crystal neutron diffraction study of heavy ice. Acta Crystallogr. 1957, **10**, 70–76.
4 H. Suga, A facet of recent ice sciences. Thermochim. Acta, 1997, **300**, 117–126.
5 H. Fukazawa, A. Hoshikawa, Y. Ishii, B. C. Chakoumakos, J. A. Fernandez-Baca, Existence of ferroelectric ice in the universe. Astrophys. J. Lett. 2006, **652**, L57–L60.
6 Y. Tajima, T. Matsuo, T. Suga, Phase transition in KOD-doped hexagonal ice. Nature, 1982, **299**, 810–812.
7 A. J. R. Leadbetter, C. Ward, J. W. Clark, P. A. Tucker, T. Matsuo, H. Suga, The equilibrium low-temperature structure of ice. J. Chem. Phys., 1985, **82**, 424–428.
8 S. Kawada, Acceleration of dielectric relaxation by KOH-doping and phase transition in ice Ih. J. Phys. Chem. Solids, 1989, **50**, 1177–1184.
9 C. M. Line, R. W. Whitworth, A high resolution neutron powder diffraction study of D_2O ice XI. J. Chem. Phys. 1996, **104**, 10008–10013.
10 A. V. Zaretskii, R. Howe, R. W. Whitworth, Dielectric studies of the transition of ice Ih to ice XI. Philos. Mag. B, 1990, **63**, 757–768.
11 H. Fukazawa, A. Hoshikawa, H. Yamauchi, Y. Yamaguchi, Y. Ishii, Formation and growth of ice XI: A powder neutron diffraction study. J. Cryst. Growth, 2005, **282**, 251–259.
12 H. Fukazawa, S. Ikeda, M. Oguro, T. Fukumura, S. Mae, Deuteron ordering in KOD-doped ice observed by neutron diffraction. J. Phys. Chem. B, 2002, **106**, 6021–6024.
13 M. A. Pick, H. Wenzl, H. Engelhardt, The specific heat of pure and doped ice near 120 °K. Z. Naturforsch. A, 1971, **26**, 810–814.
14 O. Haida, H. Suga, S. Seki, Enthalpy relaxation at glass transition temperature of heavy ice crystal. P. Jpn. Acad. 1973, **49**, 191–195.
15 O. Haida, T. Matsuo, H. Suga, S. Seki, Calorimetric study of the glassy state. X. Enthalpy relaxation at the glass-transition

ARTICLE

PCCP

temperature of hexagonal ice. J. Chem. Thermodyn., 1974, **6**, 815–825.

16 O. Haida, Enthalpy relaxation phenomenon of heavy ice. J. Glaciol. 1979, **22**, 155–164.

17 G. P. Johari, On the origin of the heat capacity feature of annealed ices and ice clathrates, and interpreting water's diffusivity in terms of the entropy. Chem. Phys. 2000, **258**, 277–290.

18 H. Fukazawa, S. Mae, S. Ikeda, O. Watanabe, Proton ordering in Antarctic ice observed by Raman and neutron scattering. Chem. Phys. Lett. 1998, **294**, 554–558.

19 H. Fukazawa, S. Mae, S. Ikeda, O. Watanabe, Incoherent inelastic neutron scattering measurements on Dome-Fuji Antarctic ice. Earth Planet. Sc. Lett. 1999, **171**, 481–487.

20 M. Arakawa, H. Kagi, H. Fukazawa, Annealing effects on hydrogen ordering in KOD-doped ice observed using neutron diffraction. J. Mol. Struct. 2010, **972**, 111–114.

21 F. Yen, Z. Chi, Proton ordering dynamics of H_2O ice. Phys. Chem. Chem. Phys. 2015, **17**, 12458.

22 A. D. Fortes, Accurate and precise lattice parameters of H_2O and D_2O ice Ih between 1.6 and 270 K from high-resolution time-of-flight neutron powder diffraction data. Acta Crystallogr. B, 2018, **74**, 196–216.

23 D. T. W. Buckingham, High-resolution thermal expansion and dielectric relaxation measurements of H_2O and D_2O ice Ih. PhD Thesis, Montana State University, 2017.

24 D. T. W. Buckingham, J. J. Neumeier, S. H. Masunaga, Y. −K. Yu, Thermal expansion of single-crystal H_2O and D_2O ice Ih. Phys. Rev. Lett., 2018, **121**, 185505.

25 R. M. Ibberson, Design and performance of the new supermirror guide on HRPD at ISIS. Nucl. Instrum. Meth. A, 2009, **600**, 47–49.

26 O. Arnold, 27 co-authors, Mantid—Data analysis and visualization package for neutron scattering and μSR experiments. Nucl. Instrum. Meth. A, 2014, **764**, 156–166.

27 A. Albinati, B. T. M. Willis, The Rietveld method in neutron and X-ray powder diffraction. J. Appl. Crystallogr. 1982, **15**, 361–374.

28 A. Le Bail, Whole powder pattern decomposition methods and applications: A retrospection. Powder Diffr. 2005, **20**, 316–326.

29 A. C. Larson, R. B. Von Dreele, General Structure Analysis System (GSAS). Los Alamos National Laboratory Report, LAUR 86-748, 1994.

30 B. H. Toby, EXPGUI, a graphical user interface for GSAS. J. Appl. Crystallogr. 2001, **34**, 210–213.

31 T. L. Malkin, B. J. Murray, C. G. Salzmann, V. Molinero, S. J. Pickering, T. F. Whale, Stacking disorder in ice I. Phys. Chem. Chem. Phys., 2015, **17**, 60–76.

32 W. I. F. David, R. M. Ibberson, T. Matsuo, High resolution neutron powder diffraction: a case study of the structure of C_{60}. P. Roy. Soc. A. Math. Phy. 1993, **442**, 129–146.

33 K. Sasaki, R. Kita, N. Shinyashiki, S. Yagihara, Dielectric relaxation time of ice-Ih with different preparation. J. Phys. Chem. B. 2016, **120**, 3950–3953.

34 L. Apekis, P. Pissis, Study of the multiplicity of dielectric relaxation times in ice at low temperatures. J. Phys. Colloq. 1987, **48**, C1–127.

35 R. P. Auty, R. H. Cole, Dielectric properties of ice and solid D_2O. J. Chem. Phys. 1952, **20**, 1309–1314.

36 S. R. Gough, D. W. Davidson, Dielectric behavior of cubic and hexagonal ices at low temperatures. J. Chem. Phys. 1970, **52**, 5442–5449.

37 A. Jeneveau, P. Sixou, Dipolar relaxation at low temperature of ice single crystal. Solid State Commun. 1972, **10**, 191–194.

38 G. P. Johari, S. J. Jones, Dielectric properties of polycrystalline D_2O ice Ih (hexagonal). P. Roy. Soc. A. Math. Phy. 1976, **349**, 467–495.

39 S. Kawada, Dielectric properties of heavy ice Ih (D_2O ice). J. Phys. Soc. Jpn. 1979, **47**, 1850–1856.

40 S. S. N. Murthy, Slow relaxation in ice and ice clathrates and its connection to the low-temperature phase transition induced by dopants. Phase Transit. 2002, **75**, 487–506.

41 Wörz, R. H. Cole, Dielectric properties of ice I. J. Chem. Phys. 1969, **51**, 1546–1551.

42 B. Geil, T. M. Kirschgen, F. Fujara, Mechanism of proton transport in hexagonal ice. Phys. Rev. B 2005, **72**, 014304.

43 I. Popov, A. Puzenko, A. Khamzin, Y. Feldman, The dynamic crossover in dielectric relaxation behavior of ice Ih. Phys. Chem. Chem. Phys. 2015, **17**, 1489–1497.

44 I. Popov, I. Lunev, A. Khamzin, A. Greenbaum, Y. Gusev, Y. Feldman, The low-temperature dynamic crossover in the dielectric relaxation of ice Ih. Phys. Chem. Chem. Phys. 2017, **19**, 28610–28620.

45 A. A. Khamzin, R R. Nigmatullin, Multiple-trapping model of dielectric relaxation of the ice Ih. J. Chem. Phys. 2017, **147**, 204502.

46 A. A. Khamzin, A. I. Nasybullin, Langevin approach to the theory of dielectric relaxation of ice Ih. Physica A. 2018, **508**, 471–480.

47 A. Khamzin, A. Nasybullin, Trap-controlled proton hopping: interpretation of low-temperature dielectric relaxation of ice Ih. Phys. Chem. Chem. Phys. 2018, **20**, 23142–23150.

48 J. P. Devlin, V. Buch, Evidence for the surface origin of point defects in ice: Control of interior proton activity by adsorbates. J. Chem. Phys. 2007, **127**, 091101.

49 N. Uras-Aytemiz, C. Joyce, J. P. Devlin, Protonic and Bjerrum defect activity near the surface of ice at T< 145 K. J. Chem. Phys., 2001, **115**, 9835–9842.

50 L. G. MacDowell, E. Sanz, C. Vega, J. L. F. Abascal, Combinatorial entropy and phase diagram of partially ordered ice phases. J. Chem. Phys., 2004, **121**, 10145–10158.

51 R. Howe, R. W. Whitworth, The configurational entropy of partially ordered ice. J. Chem. Phys. 1987, **86**, 6443–6445.

52 A. D. Fortes, I. G. Wood, D. Grigoriev, M. Alfredsson, S. Kipfstuhl, K. S. Knight, R. I. Smith, No evidence for large-scale proton ordering in Antarctic ice from powder neutron diffraction. J. Chem. Phys. 2004, **120**, 11376–11379.

53 F. Fillaux, The quantum phase-transitions of water. Europhys. Lett. 2017, **119**, 40008.

54 A. C. Neto, P. Pujol, E. Fradkin, Ice: a strongly correlated proton system. Phys. Rev. B 2006, **74**, 024302.

55 H. M. Thomas, G. E. Morfill, Melting dynamics of a plasma crystal. Nature 1996, **379**, 806–809.

56 J. C. Li, V. M. Nield, D. K. Ross, R. W. Whitworth, C. C. Wilson, D. A. Keen, Diffuse neutron-scattering study of deuterated ice Ih. Philos. Mag. B 1994, **69**, 1173–1181.

57 V. M. Nield, R. W. Whitworth, The structure of ice Ih from analysis of single-crystal neutron diffuse scattering. J. Phys. Cond. Matt. 1995, **7**, 8259–8271.

58 M. N. Beverley, V. M. Nield, Extensive tests on the application of reverse Monte Carlo modelling to single-crystal neutron diffuse scattering from ice Ih. J. Phys. Cond. Matt. 1997, **9**, 5145–5156.

59 B. Wehinger, D. Chernyshov, M. Krisch, S. Bulat, V. Ezhov, A. Bosak, Diffuse scattering in Ih ice. J. Phys. Cond. Matt. 2014, **26**, 265401.

60 L. Temleitner, L. Pusztai, Investigation of the structural disorder in ice Ih using neutron diffraction and Reverse Monte Carlo modelling. In, Physics & Chemistry of Ice (W. F. Kuhs, Ed). 593–600, 2007.

61 H. Y. Playford, T. F. Whale, B. Murray, M. G. Tucker, C. G. Salzmann, Analysis of stacking disorder in ice I using pair distribution functions. J. Appl. Crystallogr. 2018, **51**, 1211–1220.

Please do not adjust margins

Table of contents entry

High precision lattice-parameter measurements provide a potential roadmap to producing partially-ordered states of water ice.
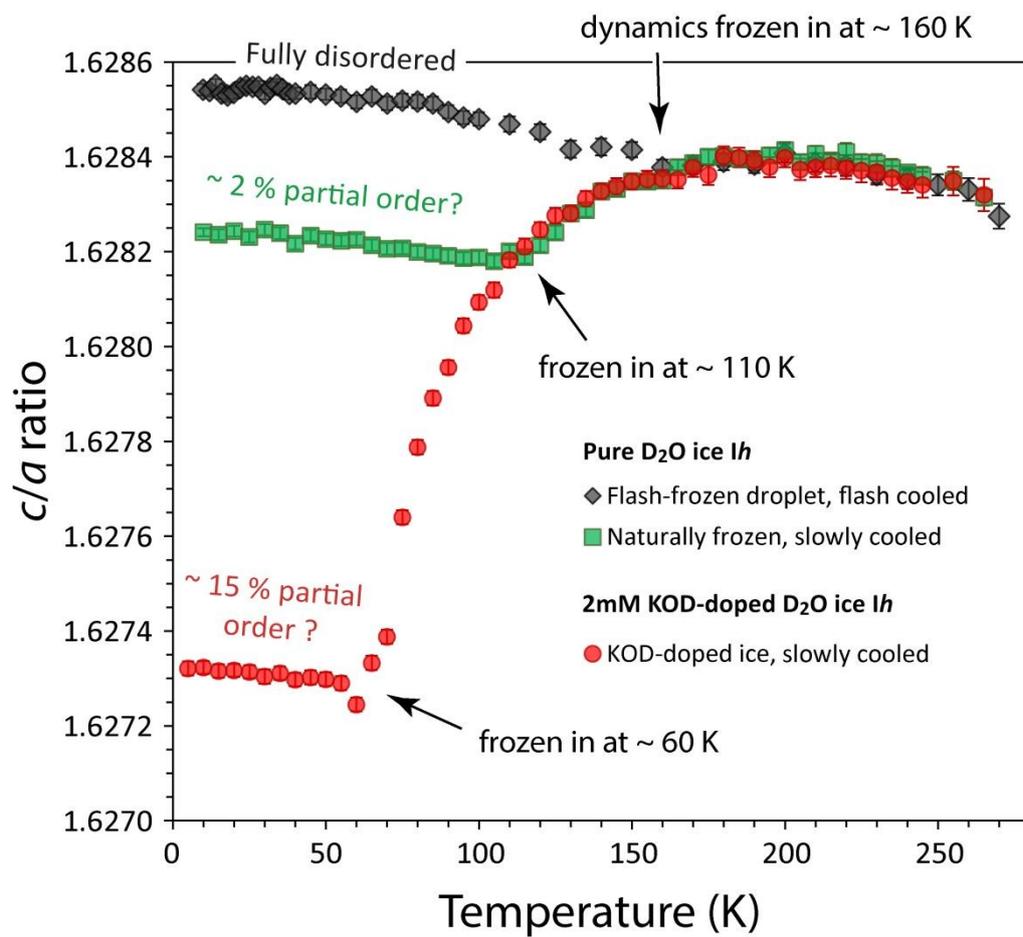
Electronic Supplementary Information

Structural manifestation of partial proton ordering and defect mobility in ice I*h*

A. Dominic Fortes,[1,2,*]

[1] ISIS Neutron & Muon Spallation Source, Rutherford Appleton Laboratory, Harwell Science and Innovation Campus, Chilton, Oxfordshire, OX11 0QX, United Kingdom.
[2] Department of Earth Sciences, University College London, Gower Street, London WC1E 6BT, United Kingdom.

*Corresponding author email: dominic.fortes@stfc.ac.uk

Contents

Section S1: Further experimental methodology – list of measurement series

Three separately-prepared samples of D_2O ice Ih were studied over a nine-day period at the end of June 2018, subdivided below into a series of different thermal protocols comprising measurements at 201 discrete temperature points (Series 1 – 5 detailed below).

The raw data is archived at doi:10.5286/ISIS.E.95699847.

A single sample of KOD-doped ice Ih was studied over a three-day period at the end of September 2018, again with a series of applied thermal protocols, comprising 86 discrete temperature points (Series 6 & 7 detailed below).

The raw data is archived at doi:10.5286/ISIS.E.98018903.

The refined lattice parameters, derived c/a ratios and the derived linear and volume thermal expansion coefficients are tabulated in the Supplementary Data Tables S1 and S2.

Series 1 (naturally-frozen ice, slowly cooled then slowly warmed)

The sample was mounted in the CCR at ~ 80 K and warmed over the space of ~ 1 hr to 240 K. Data were collected in 10 K increments on cooling to 10 K, counting for ~ 13 minutes of real time (10 µA of integrated proton current). Data were collected for 1 hr (40 µA) at 10 K. Measurements were then made on warming from 15 to 265 K in 10 K increments, interleaved with the slow-cool measurements, counting each for 10 µA.

Series 2 (LN$_2$-quench / warm / re-cool)

After the measurement at 265 K was completed, the sample stick was removed from the cryostat and the sample holder was directly immersed in liquid nitrogen. Cooling of the Al-alloy cell was observed to occur at a rate of −170 K min^{-1}, after which the sample was left immersed in LN$_2$ for ~ 1 hr whilst the CCR temperature was brought down to 80 K. The sample stick was then re-inserted and cooled to 10 K over the course of another hour. From 10 K the sample was warmed in 10 K increments to 250 K and then re-cooled in 10 K increments back down to 100 K, 20 K increments from 80 – 20 K with a final measurement at 10 K.

Series 3 (Fast cool from 170 K / warm)

From 10 K, the sample was warmed at 3 K min^{-1} to 170 K whilst maintaining the background temperature of the CCR cold-head as low as possible. The sample was maintained at 170 K for 20 minutes before the heater power was cut and the cell was permitted to cool at the fastest achievable rate (15 K min^{-1}).

Data were then collected on warming in 5 K increments from 10 to 160 K and 10 K increments from 170 – 270 K.

Series 4 (Flash-frozen globule of D_2O)

The Series 1 – 3 specimen was extracted from the sample holder under liquid nitrogen, transferred to a sealed glass bottle and allowed to melt. Three days later, this liquid D_2O

sample was poured directly into a pool of liquid nitrogen to form a single polycrystalline lump. This lump of ice was ground to a powder and transferred to the same sample holder (incl. the same sensor and heater cartridge) as was used for Series $1 - 3$. This sample was inserted into the CCR at 80 K and cooled to 10 K. Following a 1 hr data collection at 10 K, further measurements were made on warming; 10 K increments were used at low and high temperatures, but 5 K increments were used in the region between 70 and 160 K.

Series 5 (Flash frozen pipette droplet)

Finally, a fresh batch of 99.96 atom % D_2O was flash frozen by pipetting droplets into liquid nitrogen, as was done in my previous experimental study. Again, this was powdered and loaded into a sample container under liquid nitrogen. The sample holder (incl. sensor and heater) was the same one used for Series $1 - 4$ above. The same thermal protocol as the previous warming runs was employed; cool quickly to 10 K, count for one hour and then warm in 10 K increments to 260 K counting for 10 µA (13 minutes) at each point.

Series 6 (KOD-doped ice, slow warm with annealing at 70 K)

The sample was loaded into the cryostat at 200 K and cooled to 1.8 K over a period of 2 hr, after which data were collected for 40 µA (1 hr). Measurements were then made in 5 K increments up to 70 K, counting each for 15 µA (21 minutes). After annealing at 70 K for 15 hr, further measurements were made on warming in 10 K increments to 270 K with counting times of 10 µA.

Series 7 (KOD-doped ice, slow cool / warm)

Upon completion of the 270 K measurement in Series 6 the sample was cooled slowly, measuring in 5 K increments to 5 K, counting for 10 µA at each point. The sample was then re-warmed to 240 K, measuring in 10 K increments for 10 µA at each datum.

Section S2: Supplementary Data Tables

Table S1: Refined lattice parameters and axial ratios of D_2O ice Ih as a function of temperature. The temperatures shown are the average of all logged data acquired during the measurement and the stated uncertainty is the standard deviation of those values. It will be observed that the standard deviations are a few times larger amongst many of the low-temperature measurements, probably because the control-PIDs are slightly sub-optimally tuned in this region. The uncertainties on the lattice parameters are those reported by *GSAS* and the uncertainties on the *c/a* ratio are propagated directly from the lattice parameter uncertainties. Note that the error bars in all of the figures report twice this value since the scatter of the observations suggests that this is a better indication of the true systematic error.

Series 1 (Naturally-frozen ice slow-cooled from 240 K)			
T (K)	*a*-axis (Å)	*c*-axis (Å)	*c/a* ratio
240.00(1)	4.519569(9)	7.359517(24)	1.628367(6)
230.00(1)	4.517231(14)	7.355797(38)	1.628386(10)
219.99(1)	4.515013(13)	7.352293(37)	1.628410(9)
210.00(1)	4.512899(12)	7.348834(33)	1.628406(8)
200.00(1)	4.510911(12)	7.345634(31)	1.628415(8)
189.99(1)	4.509071(11)	7.342545(31)	1.628394(8)
180.00(1)	4.507319(11)	7.339726(30)	1.628402(8)
169.99(1)	4.505693(11)	7.337012(31)	1.628387(8)
160.00(1)	4.504211(11)	7.334430(29)	1.628350(8)
150.00(1)	4.502830(11)	7.332175(29)	1.628348(8)
140.00(1)	4.501579(10)	7.330042(28)	1.628327(7)
130.00(1)	4.500515(10)	7.328099(27)	1.628280(7)
120.00(1)	4.499597(10)	7.326304(27)	1.628213(7)
109.99(1)	4.498757(10)	7.324879(26)	1.628201(7)
100.00(1)	4.498092(10)	7.323740(26)	1.628188(7)
89.99(1)	4.497567(10)	7.322899(25)	1.628191(7)
79.99(1)	4.497190(9)	7.322323(24)	1.628200(6)
70.00(2)	4.496980(9)	7.322012(23)	1.628206(6)
59.99(3)	4.496901(9)	7.321966(23)	1.628225(6)
50.01(2)	4.496947(9)	7.322047(23)	1.628226(6)
39.99(4)	4.497099(9)	7.322254(23)	1.628217(6)
30.01(2)	4.497291(9)	7.322698(22)	1.628246(6)
19.99(2)	4.497473(9)	7.322980(22)	1.628243(6)
9.99(2)	4.497548(6)	7.323092(16)	1.628241(4)
15.01(2)	4.497524(9)	7.323030(22)	1.628236(6)
25.00(3)	4.497388(8)	7.322788(22)	1.628231(6)
35.01(3)	4.497185(9)	7.322492(24)	1.628239(6)
45.01(4)	4.497008(9)	7.322180(23)	1.628234(6)

T (K)	a-axis (Å)	c-axis (Å)	c/a ratio
55.01(2)	4.496907(9)	7.321968(22)	1.628223(6)
65.01(2)	4.496912(9)	7.321932(23)	1.628213(6)
75.00(1)	4.497061(9)	7.322147(23)	1.628207(6)
85.00(1)	4.497354(9)	7.322573(24)	1.628196(6)
95.00(0)	4.497818(9)	7.323287(24)	1.628187(6)
105.00(1)	4.498425(9)	7.324245(25)	1.628180(6)
115.00(1)	4.499174(10)	7.325503(25)	1.628188(7)
125.01(1)	4.500038(10)	7.327145(27)	1.628241(7)
135.01(1)	4.501057(10)	7.329016(27)	1.628288(7)
145.00(1)	4.502221(11)	7.331111(29)	1.628332(8)
155.00(1)	4.503505(10)	7.333273(28)	1.628348(7)
165.01(1)	4.504921(11)	7.335716(31)	1.628378(8)
175.00(0)	4.506480(11)	7.338353(29)	1.628400(8)
185.01(1)	4.508175(12)	7.341096(32)	1.628396(8)
195.01(1)	4.509980(11)	7.344066(31)	1.628403(8)
205.00(1)	4.511921(12)	7.347162(31)	1.628389(8)
215.01(1)	4.513956(12)	7.350488(34)	1.628392(9)
225.01(1)	4.516099(12)	7.353963(34)	1.628388(9)
235.00(1)	4.518356(13)	7.357586(37)	1.628377(9)
245.00(1)	4.520746(13)	7.361402(37)	1.628360(9)
255.00(1)	4.523211(13)	7.365370(39)	1.628350(10)
265.01(1)	4.525831(12)	7.369477(35)	1.628315(9)

Series 2 (Naturally-frozen ice quenched from 265 to 77 K)

T (K)	a-axis (Å)	c-axis (Å)	c/a ratio
9.99(12)	4.497611(7)	7.323696(18)	1.628352(5)
20.00(2)	4.497493(9)	7.323450(23)	1.628340(6)
30.01(4)	4.497315(9)	7.323162(23)	1.628341(6)
39.99(3)	4.497110(9)	7.322818(25)	1.628339(6)
50.00(3)	4.496964(9)	7.322565(25)	1.628335(6)
59.99(3)	4.496912(9)	7.322409(25)	1.628319(6)
70.01(2)	4.496977(9)	7.322588(26)	1.628336(7)
80.00(3)	4.497199(9)	7.322926(25)	1.628330(6)
90.00(0)	4.497561(9)	7.323521(25)	1.628332(6)
100.00(1)	4.498103(10)	7.324309(27)	1.628311(7)
110.00(1)	4.498829(10)	7.325182(26)	1.628242(7)
120.00(1)	4.499634(10)	7.326634(26)	1.628273(7)
130.01(1)	4.500605(10)	7.328327(29)	1.628298(7)
140.00(2)	4.501701(10)	7.330170(29)	1.628311(7)
150.00(1)	4.502919(10)	7.332342(29)	1.628353(7)
160.00(1)	4.504265(10)	7.334608(29)	1.628370(7)
170.00(1)	4.505750(10)	7.337157(30)	1.628399(8)
180.01(0)	4.507390(11)	7.339809(32)	1.628394(8)
190.00(2)	4.509109(11)	7.342640(32)	1.628402(8)

200.00(1)	4.510969(11)	7.345651(33)	1.628398(8)
210.00(1)	4.512956(12)	7.348881(36)	1.628396(9)
220.00(1)	4.515025(13)	7.352359(37)	1.628420(9)
230.01(1)	4.517250(13)	7.355904(37)	1.628403(9)
240.01(1)	4.519561(13)	7.359533(38)	1.628373(10)
250.01(1)	4.521996(14)	7.363368(40)	1.628345(10)
240.00(1)	4.519563(13)	7.359479(38)	1.628361(10)
230.00(1)	4.517232(13)	7.355777(37)	1.628381(9)
219.99(1)	4.515044(12)	7.352214(36)	1.628381(9)
210.00(1)	4.512934(13)	7.348891(36)	1.628406(9)
200.00(1)	4.510942(12)	7.345628(34)	1.628402(9)
190.00(1)	4.509124(12)	7.342620(35)	1.628392(9)
180.00(1)	4.507343(11)	7.339763(32)	1.628401(8)
169.99(1)	4.505716(11)	7.337057(31)	1.628389(8)
160.00(1)	4.504226(11)	7.334582(31)	1.628378(8)
150.00(1)	4.502885(11)	7.332214(30)	1.628337(8)
140.00(1)	4.501644(10)	7.330155(29)	1.628328(7)
130.00(1)	4.500551(10)	7.328222(28)	1.628294(7)
120.00(2)	4.499623(10)	7.326375(27)	1.628220(7)
109.99(2)	4.498803(10)	7.324973(26)	1.628205(7)
99.99(3)	4.498123(10)	7.323853(26)	1.628202(7)
79.99(3)	4.497226(9)	7.322398(25)	1.628203(6)
59.98(3)	4.496933(9)	7.321901(24)	1.628199(6)
40.00(3)	4.497140(9)	7.322317(24)	1.628216(6)
20.00(2)	4.497507(9)	7.322958(23)	1.628226(6)
10.00(3)	4.497593(7)	7.323126(19)	1.628232(5)

Series 3 (Ice warmed to 170 K and cooled at 15 K min^{-1})

T (K)	a-axis (Å)	c-axis (Å)	c/a ratio
170.01(6)	4.506146(12)	7.337701(34)	1.628376(9)
10.00(2)	4.497551(7)	7.323407(18)	1.628310(5)
15.00(2)	4.497524(9)	7.323379(23)	1.628313(6)
19.99(2)	4.497471(9)	7.323300(23)	1.628315(6)
25.00(3)	4.497392(8)	7.323124(23)	1.628305(6)
30.00(3)	4.497279(9)	7.322963(23)	1.628310(6)
34.99(2)	4.497181(9)	7.322805(24)	1.628310(6)
40.00(4)	4.497107(9)	7.322626(23)	1.628297(6)
45.01(2)	4.497014(9)	7.322487(24)	1.628300(6)
50.01(3)	4.496941(9)	7.322398(24)	1.628306(6)
55.01(3)	4.496905(9)	7.322256(24)	1.628288(6)
60.00(3)	4.496902(9)	7.322203(25)	1.628277(6)
65.01(4)	4.496922(10)	7.322206(26)	1.628271(7)
70.01(3)	4.496969(9)	7.322285(24)	1.628271(6)

75.00(4)	4.497058(9)	7.322491(25)	1.628285(6)
79.99(3)	4.497177(9)	7.322667(25)	1.628281(6)
84.99(3)	4.497357(9)	7.322949(25)	1.628278(6)
90.00(1)	4.497565(9)	7.323245(26)	1.628269(7)
95.00(1)	4.497809(10)	7.323631(26)	1.628266(7)
100.00(1)	4.498090(10)	7.324071(26)	1.628262(7)
105.00(1)	4.498411(10)	7.324543(27)	1.628251(7)
110.00(1)	4.498782(10)	7.325027(27)	1.628224(7)
115.01(1)	4.499218(10)	7.325639(27)	1.628203(7)
120.00(1)	4.499621(10)	7.326415(29)	1.628229(7)
125.01(1)	4.500095(11)	7.327222(30)	1.628237(8)
130.01(1)	4.500576(10)	7.328137(29)	1.628266(7)
135.00(1)	4.501083(11)	7.329108(31)	1.628299(8)
140.00(1)	4.501642(11)	7.330134(29)	1.628325(8)
145.00(1)	4.502235(11)	7.331114(29)	1.628328(8)
150.00(1)	4.502856(11)	7.332276(30)	1.628361(8)
155.00(1)	4.503544(11)	7.333416(30)	1.628366(8)
160.00(1)	4.504247(11)	7.334546(30)	1.628362(8)
170.00(1)	4.505708(11)	7.337052(32)	1.628390(8)
180.01(0)	4.507320(11)	7.339752(32)	1.628407(8)
190.00(1)	4.509081(12)	7.342551(34)	1.628392(9)
200.01(1)	4.510931(12)	7.345648(33)	1.628411(9)
210.00(1)	4.512907(12)	7.348823(34)	1.628401(9)
220.00(1)	4.515018(12)	7.352220(35)	1.628392(9)
230.00(1)	4.517230(13)	7.355753(37)	1.628377(9)
240.01(1)	4.519569(14)	7.359488(39)	1.628361(10)
250.01(1)	4.521977(14)	7.363389(40)	1.628356(10)
260.01(1)	4.524534(14)	7.367392(40)	1.628321(10)
270.01(1)	4.527212(11)	7.371622(33)	1.628292(8)

Series 4 (Flash frozen D_2O globule)

T (K)	a-axis (Å)	c-axis (Å)	c/a ratio
9.99(3)	4.497540(8)	7.323524(21)	1.628340(5)
20.00(3)	4.497474(9)	7.323407(24)	1.628338(6)
30.00(3)	4.497291(9)	7.323134(24)	1.628343(6)
39.99(3)	4.497096(10)	7.322797(25)	1.628339(7)
50.00(3)	4.496942(9)	7.322484(25)	1.628325(6)
60.00(2)	4.496879(10)	7.322349(26)	1.628318(7)
70.00(1)	4.496945(10)	7.322481(25)	1.628323(7)
75.00(2)	4.497047(10)	7.322581(26)	1.628309(7)
80.00(1)	4.497181(10)	7.322754(26)	1.628299(7)
85.00(1)	4.497342(10)	7.322976(27)	1.628290(7)
90.00(1)	4.497553(10)	7.323335(26)	1.628293(7)
95.00(1)	4.497815(10)	7.323602(26)	1.628258(7)

100.00(1)	4.498125(10)	7.324005(26)	1.628235(7)
105.00(1)	4.498418(11)	7.324532(28)	1.628246(7)
110.00(1)	4.498778(11)	7.325138(28)	1.628251(7)
115.00(1)	4.499170(11)	7.325819(28)	1.628260(7)
120.00(1)	4.499596(11)	7.326530(29)	1.628264(8)
125.01(1)	4.500047(11)	7.327298(28)	1.628271(7)
130.01(1)	4.500551(12)	7.328145(30)	1.628277(8)
135.01(1)	4.501080(11)	7.329075(30)	1.628293(8)
140.01(1)	4.501640(11)	7.330070(30)	1.628311(8)
145.01(1)	4.502239(12)	7.331111(30)	1.628326(8)
150.01(1)	4.502863(12)	7.332233(32)	1.628349(8)
155.00(1)	4.503526(11)	7.333333(30)	1.628354(8)
160.00(1)	4.504221(12)	7.334540(31)	1.628370(8)
170.00(1)	4.505713(12)	7.337105(32)	1.628400(8)
180.00(1)	4.507348(12)	7.339719(32)	1.628390(8)
190.01(1)	4.509095(12)	7.342600(32)	1.628398(8)
200.00(1)	4.510942(13)	7.345660(34)	1.628409(9)
210.01(2)	4.512963(13)	7.348841(37)	1.628385(9)
220.00(1)	4.515051(13)	7.352252(36)	1.628387(9)
230.00(1)	4.517266(13)	7.355794(36)	1.628373(9)
240.01(1)	4.519610(14)	7.359577(39)	1.628366(10)
250.01(1)	4.522040(14)	7.363491(37)	1.628356(10)
260.00(1)	4.524590(15)	7.367566(40)	1.628339(10)
270.01(1)	4.527267(16)	7.371748(45)	1.628300(11)

Series 5 (Flash frozen D_2O droplet)

T (K)	a-axis (Å)	c-axis (Å)	c/a ratio
9.99(3)	4.497443(7)	7.323987(17)	1.628478(5)
20.00(3)	4.497348(9)	7.323858(23)	1.628484(6)
30.01(4)	4.497182(9)	7.323533(24)	1.628472(6)
40.00(4)	4.496997(9)	7.323247(24)	1.628475(6)
50.01(3)	4.496826(10)	7.322956(25)	1.628472(7)
60.00(3)	4.496792(9)	7.322798(24)	1.628449(6)
70.01(3)	4.496865(10)	7.322883(25)	1.628442(7)
80.00(3)	4.497088(10)	7.323181(27)	1.628427(7)
90.00(1)	4.497476(10)	7.323749(27)	1.628413(7)
100.00(1)	4.498002(10)	7.324630(27)	1.628419(7)
110.01(1)	4.498709(10)	7.325554(27)	1.628368(7)
120.00(1)	4.499577(12)	7.326591(32)	1.628284(8)
130.01(1)	4.500546(11)	7.328178(29)	1.628286(8)
140.00(1)	4.501663(11)	7.330067(30)	1.628302(8)
150.01(1)	4.502846(12)	7.332240(31)	1.628357(8)
160.00(1)	4.504230(12)	7.334548(33)	1.628369(9)
170.00(1)	4.505709(13)	7.337081(34)	1.628397(9)

180.01(1)	4.507341(12)	7.339767(33)	1.628403(9)
190.01(1)	4.509079(13)	7.342655(34)	1.628416(9)
200.00(1)	4.510922(13)	7.345695(37)	1.628424(9)
210.00(1)	4.512921(13)	7.348836(36)	1.628399(9)
220.00(1)	4.515021(13)	7.352251(38)	1.628398(10)
230.01(1)	4.517223(13)	7.355812(36)	1.628392(9)
240.00(1)	4.519558(13)	7.359517(36)	1.628371(9)
250.01(1)	4.522012(14)	7.363430(37)	1.628353(10)
260.00(1)	4.524569(15)	7.367425(41)	1.628315(11)

Series 6 (Slowly warmed KOD-doped ice with anneal at 70 K)

T (K)	a-axis (Å)	c-axis (Å)	c/a ratio
1.84(5)	4.497813(7)	7.319160(19)	1.627271(9)
4.99(1)	4.497821(9)	7.319192(24)	1.627275(13)
10.08(1)	4.497809(9)	7.319133(23)	1.627266(12)
14.97(3)	4.497781(9)	7.319114(23)	1.627272(12)
19.94(1)	4.497777(10)	7.319087(24)	1.627268(13)
24.76(1)	4.497712(10)	7.318954(24)	1.627262(13)
30.08(6)	4.497620(9)	7.318781(23)	1.627256(12)
35.19(1)	4.497503(9)	7.318630(24)	1.627265(13)
40.08(1)	4.497415(9)	7.318400(24)	1.627246(13)
45.00(1)	4.497334(9)	7.318289(24)	1.627250(13)
50.12(1)	4.497284(10)	7.318118(24)	1.627231(13)
55.24(1)	4.497248(10)	7.317956(26)	1.627208(14)
60.17(1)	4.497277(10)	7.317647(26)	1.627128(14)
65.21(1)	4.497333(10)	7.317556(26)	1.627088(14)
70.00(1)	4.497388(15)	7.317151(39)	1.626978(20)
80.00(1)	4.497238(11)	7.320335(29)	1.627740(15)
90.01(1)	4.497482(11)	7.321729(28)	1.627962(15)
100.01(1)	4.497957(11)	7.323074(29)	1.628089(15)
110.00(1)	4.498605(12)	7.324560(30)	1.628185(16)
120.01(1)	4.499408(11)	7.326199(30)	1.628258(16)
130.00(1)	4.500384(12)	7.327915(31)	1.628287(16)
140.00(2)	4.501472(12)	7.329884(31)	1.628330(16)
150.00(3)	4.502710(12)	7.332078(33)	1.628370(17)
160.01(1)	4.504116(12)	7.334342(33)	1.628364(17)
170.00(1)	4.505632(13)	7.336957(34)	1.628397(18)
180.00(1)	4.507294(13)	7.339676(35)	1.628400(18)
190.01(1)	4.509017(14)	7.342603(36)	1.628427(19)
200.00(1)	4.510927(14)	7.345639(37)	1.628410(19)
210.00(2)	4.512947(14)	7.348866(38)	1.628396(20)
220.00(1)	4.515059(14)	7.352415(39)	1.628421(20)

230.01(2)	4.517354(15)	7.355896(41)	1.628364(21)
240.00(2)	4.519708(16)	7.359623(45)	1.628340(23)
250.01(1)	4.522182(17)	7.363607(47)	1.628331(24)
260.00(2)	4.524754(19)	7.367703(51)	1.628310(26)
270.00(1)	4.527396(24)	7.371922(63)	1.628292(33)

Series 7 (Slowly cooled / warmed KOD-doped ice)

T (K)	a-axis (Å)	c-axis (Å)	c/a ratio
265.00(3)	4.525950(24)	7.369694(66)	1.628320(34)
255.00(1)	4.523293(22)	7.365499(58)	1.628349(30)
244.99(2)	4.520751(20)	7.361325(52)	1.628341(27)
235.00(1)	4.518391(18)	7.357548(48)	1.628356(25)
225.00(1)	4.516061(18)	7.353823(47)	1.628371(25)
215.00(1)	4.513867(17)	7.350299(44)	1.628382(23)
205.00(1)	4.511825(16)	7.346937(44)	1.628374(23)
195.00(1)	4.509871(16)	7.343777(40)	1.628379(21)
184.99(1)	4.508049(15)	7.340900(39)	1.628398(20)
174.99(1)	4.506337(15)	7.337946(40)	1.628362(21)
165.00(1)	4.504775(14)	7.335363(36)	1.628353(19)
155.00(1)	4.503253(13)	7.332884(34)	1.628353(18)
144.99(1)	4.501885(13)	7.330589(33)	1.628338(17)
134.99(2)	4.500772(12)	7.328660(32)	1.628312(17)
125.00(1)	4.499751(12)	7.326837(32)	1.628276(17)
114.99(1)	4.498870(12)	7.325110(32)	1.628211(17)
104.99(1)	4.498193(12)	7.323595(31)	1.628119(16)
94.99(1)	4.497611(11)	7.322309(29)	1.628044(15)
84.99(1)	4.497238(11)	7.321014(29)	1.627891(15)
75.00(2)	4.497072(11)	7.319615(28)	1.627640(15)
64.99(2)	4.497106(11)	7.318288(29)	1.627333(15)
54.98(2)	4.497106(11)	7.318096(28)	1.627290(15)
45.00(2)	4.497201(11)	7.318306(28)	1.627302(15)
35.00(2)	4.497386(11)	7.318646(27)	1.627311(14)
25.03(4)	4.497572(10)	7.318962(27)	1.627314(14)
15.01(2)	4.497693(11)	7.319166(26)	1.627316(14)
5.00(2)	4.497707(11)	7.319215(28)	1.627321(15)
10.02(4)	4.497706(10)	7.319221(26)	1.627323(14)
20.00(2)	4.497645(10)	7.319094(26)	1.627317(14)
29.99(3)	4.497486(11)	7.318778(29)	1.627304(15)
39.99(2)	4.497293(11)	7.318434(27)	1.627298(14)
50.00(1)	4.497132(11)	7.318176(27)	1.627298(14)
60.00(1)	4.497116(11)	7.317911(28)	1.627245(15)
70.00(1)	4.497123(11)	7.318563(28)	1.627388(15)
80.00(1)	4.497129(11)	7.320371(29)	1.627788(15)

90.01(1)	4.497444(11)	7.321641(28)	1.627956(15)
100.00(1)	4.497889(11)	7.322983(29)	1.628093(15)
110.01(1)	4.498539(11)	7.324442(30)	1.628182(16)
120.01(1)	4.499334(12)	7.326024(30)	1.628246(16)
130.00(1)	4.500333(12)	7.327808(32)	1.628281(17)
140.00(1)	4.501419(12)	7.329784(32)	1.628327(17)
150.00(1)	4.502687(13)	7.331942(33)	1.628348(17)
160.01(1)	4.504088(14)	7.334249(36)	1.628354(19)
170.00(1)	4.505622(14)	7.336852(37)	1.628377(19)
180.00(1)	4.507244(15)	7.339604(38)	1.628402(20)
190.01(1)	4.509048(15)	7.342498(39)	1.628392(20)
200.00(1)	4.510901(15)	7.345543(39)	1.628398(20)
210.00(2)	4.512918(15)	7.348736(39)	1.628378(20)
220.00(1)	4.515020(16)	7.352149(42)	1.628376(22)
230.01(2)	4.517287(17)	7.355804(44)	1.628368(23)
240.00(1)	4.519639(17)	7.359545(47)	1.628348(24)

Table S2: Calculated linear and volume thermal expansion coefficients as a function of temperature.

Series 1 (Naturally-frozen ice slow-cooled from 240 K)

T (K)	α_a (x10^6 K^{-1})	α_c (x10^6 K^{-1})	α_V (x10^6 K^{-1})
230	50.4(7)	49.1(5)	149.9(9)
220	47.9(9)	47.3(7)	143.2(11)
210	45.4(9)	45.3(6)	136.1(11)
200	42.4(8)	42.8(6)	127.6(10)
190	39.8(8)	40.2(6)	119.8(10)
180	37.5(8)	37.7(5)	112.6(9)
170	34.5(8)	36.1(5)	105.0(9)
160	31.8(8)	33.0(5)	96.5(9)
150	29.2(7)	29.9(5)	88.3(9)
140	25.7(7)	27.8(5)	79.2(9)
130	22.0(7)	25.5(5)	69.5(9)
120	19.5(7)	22.0(5)	61.0(8)
110	16.7(7)	17.5(5)	50.9(8)
100	13.2(7)	13.5(5)	40.0(8)
90	10.0(7)	9.7(5)	29.7(8)
80	6.5(6)	6.1(5)	19.1(8)
70	3.2(6)	2.4(4)	8.9(7)
60	0.4(6)	−0.2(4)	0.5(7)
50	−2.2(6)	−2.0(4)	−6.4(7)
40	−3.8(6)	−4.4(4)	−12.1(7)
30	−4.2(6)	−5.0(4)	−13.3(7)
20	−2.9(5)	−2.7(4)	−8.4(7)
25	−3.8(6)	−3.7(4)	−11.2(7)
35	−4.2(6)	−4.2(4)	−12.6(7)
45	−3.1(6)	−3.6(4)	−9.8(7)
55	−1.1(6)	−1.7(4)	−3.8(7)
65	1.7(6)	1.2(4)	4.6(7)
75	4.9(6)	4.4(4)	14.2(7)
85	8.4(6)	7.8(4)	24.6(7)
95	11.9(6)	11.4(4)	35.2(8)
105	15.1(6)	15.1(4)	45.3(8)
115	17.9(6)	19.8(4)	55.7(8)
125	20.9(7)	24.0(5)	65.8(8)
135	24.3(7)	27.1(5)	75.6(9)
145	27.2(7)	29.0(5)	83.4(8)
155	30.0(8)	31.4(5)	91.4(9)
165	33.0(7)	34.6(5)	100.7(9)

175	36.1(8)	36.7(5)	108.9(10)
185	38.8(7)	38.9(5)	116.6(9)
195	41.5(8)	41.3(6)	124.4(10)
205	44.1(8)	43.7(6)	131.9(10)
215	46.3(8)	46.3(6)	138.9(10)
225	48.7(9)	48.3(6)	145.8(11)
235	51.4(9)	50.6(6)	153.5(11)
245	53.7(9)	52.9(7)	160.3(11)
255	56.2(9)	54.8(6)	167.3(11)

Series 2 (Naturally-frozen ice quenched from 265 to 77 K)

T (K)	α_a (x10^6 K^{-1})	α_c (x10^6 K^{-1})	α_V (x10^6 K^{-1})
20	−3.3(5)	−3.6(3)	−10.2(6)
30	−4.3(6)	−4.3(4)	−12.8(7)
40	−3.9(6)	−4.1(4)	−11.9(7)
50	−2.2(6)	−2.8(4)	−7.2(8)
60	0.1(6)	0.2(4)	0.4(8)
70	3.2(6)	3.5(4)	9.9(8)
80	6.5(6)	6.4(5)	19.4(8)
90	10.1(6)	9.4(4)	29.5(8)
100	14.1(6)	11.3(4)	39.5(8)
110	17.0(7)	15.9(5)	49.9(8)
120	19.7(7)	21.5(5)	60.9(8)
130	23.0(7)	24.1(5)	70.1(8)
140	25.7(7)	27.4(5)	78.8(9)
150	28.5(7)	30.3(5)	87.2(9)
160	31.4(7)	32.8(5)	95.7(9)
170	34.7(7)	35.5(5)	104.8(9)
180	37.3(7)	37.4(5)	111.9(9)
190	39.7(8)	39.8(6)	119.2(10)
200	42.7(8)	42.5(6)	127.8(10)
210	45.0(8)	45.7(6)	135.6(10)
220	47.6(9)	47.8(6)	142.9(11)
230	50.2(9)	48.8(7)	149.3(11)
240	52.5(9)	50.7(7)	155.8(11)
230	50.0(9)	49.4(7)	149.3(11)
220	47.6(9)	46.8(8)	142.0(11)
210	45.4(9)	44.8(6)	135.6(11)
200	42.2(9)	42.7(6)	127.1(11)
190	39.9(8)	39.9(6)	119.7(10)
180	37.8(8)	37.9(6)	113.5(10)
170	34.6(8)	35.3(6)	104.4(10)

160	31.4(8)	33.0(6)	95.8(9)
150	28.7(8)	30.2(6)	87.5(9)
140	25.9(7)	27.2(6)	79.1(9)
130	22.4(7)	25.8(6)	70.7(9)
120	19.4(7)	22.2(6)	61.0(8)
110	16.7(7)	17.2(6)	50.5(8)
95	11.7(4)	11.7(3)	35.1(5)
80	6.6(3)	6.7(2)	19.9(4)
60	0.5(3)	0.3(2)	1.2(4)
40	−3.2(3)	−3.6(2)	−10.0(4)
25	−3.4(4)	−3.7(3)	−10.4(5)

Series 3 (Ice warmed to 170 K and cooled at 15 K min^{-1})

T (K)	α_a (x10^6 K^{-1})	α_c (x10^6 K^{-1})	α_V (x10^6 K^{-1})
15	−1.8(10)	−1.5(7)	−5.0(12)
20	−2.9(12)	−3.5(8)	−9.4(14)
25	−4.3(12)	−4.6(8)	−13.1(15)
30	−4.7(12)	−4.4(8)	−13.7(14)
35	−3.8(12)	−4.6(8)	−12.3(15)
40	−3.7(12)	−4.3(9)	−11.8(15)
45	−3.7(12)	−3.1(9)	−10.5(15)
50	−2.4(12)	−3.2(9)	−8.0(15)
55	−0.9(12)	−2.7(9)	−4.4(15)
60	0.4(13)	−0.7(9)	0.1(15)
65	1.5(12)	1.1(9)	4.1(15)
70	3.0(13)	3.9(9)	9.9(16)
75	4.6(12)	5.2(9)	14.5(15)
80	6.6(13)	6.3(9)	19.6(15)
85	8.6(13)	7.9(9)	25.1(15)
90	10.1(13)	9.3(9)	29.4(16)
95	11.7(13)	11.3(9)	34.6(16)
100	13.4(13)	12.5(10)	39.2(17)
105	15.4(13)	13.1(10)	43.8(17)
110	17.9(14)	15.0(10)	50.8(17)
115	18.6(14)	18.9(10)	56.2(17)
120	19.5(14)	21.6(10)	60.6(17)
125	21.2(14)	23.5(10)	66.0(18)
130	22.0(15)	25.7(11)	69.6(19)
135	23.7(15)	27.3(10)	74.6(18)
140	25.6(15)	27.4(11)	78.6(19)
145	27.0(15)	29.2(11)	83.2(18)
150	29.1(15)	31.4(11)	89.5(18)
155	30.9(15)	31.0(11)	92.7(19)
162.5	32.0(10)	33.1(7)	97.1(12)

170	34.1(8)	35.5(5)	103.7(9)
180	37.4(8)	37.5(6)	112.3(10)
190	40.1(8)	40.2(6)	120.3(10)
200	42.4(8)	42.7(6)	127.6(10)
210	45.3(8)	44.7(6)	135.3(10)
220	47.9(9)	47.2(6)	142.9(11)
230	50.4(9)	49.4(6)	150.2(11)
240	52.5(9)	51.9(7)	157.0(11)
250	54.9(10)	53.7(7)	163.6(12)
260	57.9(9)	55.9(7)	171.7(12)

Series 4 (Flash frozen D_2O globule)

T (K)	α_a (x10^6 K^{-1})	α_c (x10^6 K^{-1})	α_V (x10^6 K^{-1})
20	−2.8(6)	−2.7(4)	−8.2(7)
30	−4.2(6)	−4.2(4)	−12.6(8)
40	−3.9(6)	−4.4(4)	−12.2(8)
50	−2.4(7)	−3.1(5)	−7.9(8)
60	0.0(6)	0.0(4)	0.0(8)
67.5	2.5(9)	2.1(6)	7.1(11)
75	5.2(13)	3.7(9)	14.2(16)
80	6.6(13)	5.4(10)	18.5(17)
85	8.3(13)	7.9(9)	24.5(16)
90	10.5(14)	8.5(10)	29.6(17)
95	12.7(13)	9.1(9)	34.6(16)
100	13.4(14)	12.7(10)	39.5(17)
105	14.5(14)	15.5(10)	44.5(17)
110	16.7(15)	17.6(10)	51.0(18)
115	18.2(15)	19.0(10)	55.4(18)
120	19.5(15)	20.2(10)	59.2(18)
125	21.2(15)	22.0(11)	64.5(18)
130	23.0(15)	24.3(10)	70.2(18)
135	24.2(16)	26.3(11)	74.7(19)
140	25.7(15)	27.8(11)	79.3(19)
145	27.2(16)	29.5(11)	83.8(19)
150	28.6(16)	30.3(11)	87.5(19)
155	30.2(16)	31.5(11)	91.8(20)
162.5	32.4(10)	34.3(7)	99.0(13)
170	34.7(8)	35.3(6)	104.7(10)
180	37.5(8)	37.4(6)	112.5(10)
190	39.9(8)	40.5(6)	120.2(10)
200	42.9(8)	42.5(6)	128.3(10)
210	45.5(9)	44.9(6)	136.0(11)
220	47.7(9)	47.3(6)	142.7(11)

230	50.5(9)	49.8(6)	150.8(11)
240	52.8(9)	52.3(6)	158.0(11)
250	55.1(10)	54.3(7)	164.5(12)
260	57.8(10)	56.1(7)	171.7(12)

Series 5 (Flash frozen D_2O droplet)

T (K)	α_a (x10^6 K^{-1})	α_c (x10^6 K^{-1})	α_V (x10^6 K^{-1})
20	−2.9(5)	−3.1(3)	−8.9(6)
30	−3.9(6)	−4.2(4)	−12.0(7)
40	−4.0(6)	−3.9(4)	−11.9(8)
50	−2.3(6)	−3.1(4)	−7.6(7)
60	0.4(7)	−0.5(5)	0.4(8)
70	3.3(6)	2.6(4)	9.2(8)
80	6.8(7)	5.9(5)	19.5(8)
90	10.2(7)	9.9(5)	30.2(8)
100	13.7(7)	12.3(5)	39.7(8)
110	17.5(7)	13.4(5)	48.4(9)
120	20.4(7)	17.9(5)	58.7(9)
130	23.2(8)	23.7(6)	70.1(10)
140	25.6(8)	27.7(5)	78.8(9)
150	28.5(8)	30.6(5)	87.6(10)
160	31.8(8)	33.0(6)	96.6(10)
170	34.5(8)	35.6(6)	104.6(10)
180	37.4(9)	38.0(6)	112.8(11)
190	39.7(9)	40.4(6)	119.8(10)
200	42.6(9)	42.1(6)	127.3(11)
210	45.4(9)	44.6(7)	135.5(11)
220	47.7(9)	47.5(6)	142.8(11)
230	50.2(9)	49.4(7)	149.9(11)
240	53.0(9)	51.8(6)	157.8(11)
250	55.4(9)	53.7(7)	164.6(11)

Series 6 (Slowly warmed KOD-doped ice with anneal at 70 K)

T (K)	α_a (x10^6 K^{-1})	α_c (x10^6 K^{-1})	α_V (x10^6 K^{-1})
3.42	0.6(33)	1.4(23)	3(4)
7.54	−0.5(24)	−1.6(17)	−3(3)
12.52	−1.3(24)	−0.5(17)	−3(3)
17.45	−0.2(25)	−0.7(17)	−1(3)
22.35	−3.0(27)	−3.8(19)	−10(3)
27.42	−3.8(24)	−4.4(17)	−12(3)

32.64	−5.1(24)	−4.1(17)	−14(3)
37.64	−4.0(25)	−6.4(18)	−14(3)
42.54	−3.7(25)	−3.1(18)	−10(3)
47.56	−2.2(24)	−4.6(17)	−9(3)
52.68	−1.6(25)	−4.3(18)	−7(3)
57.71	1.3(27)	−8.6(19)	−6(3)
62.69	2.5(27)	−2.5(19)	2(3)
75	−3.3(19)	43.5(14)	36.8(23)
85	5.4(15)	19.0(10)	29.9(18)
95	10.6(15)	18.4(10)	39.5(18)
105	14.4(15)	20.3(11)	49.1(18)
115	17.8(16)	22.4(11)	58.0(19)
125	21.7(15)	23.4(11)	66.9(19)
135	24.2(16)	26.9(11)	75(2)
145	27.5(16)	30.0(11)	85(2)
155	31.2(17)	30.8(12)	93(2)
165	33.7(17)	35.7(12)	103(2)
175	36.9(18)	37.1(12)	111(2)
185	38.2(18)	39.8(13)	116(2)
195	42.4(19)	41.4(13)	126(2)
205	44.8(19)	43.9(13)	133(2)
215	47(2)	48.3(14)	142(2)
225	51(2)	47.3(14)	149(2)
235	52(2)	50.7(15)	155(3)
245	55(2)	54.1(16)	163(3)
255	57(2)	55.7(17)	170(3)
265	58(3)	57.3(19)	174(3)

Series 7 (Slowly cooled / warmed KOD-doped ice)

T (K)	α_a (x10^6 K^{-1})	α_c (x10^6 K^{-1})	α_V (x10^6 K^{-1})
260	59(3)	57(2)	174(4)
250	56(3)	57(2)	169(4)
240	52(3)	51.3(19)	156(3)
230	52(2)	50.6(17)	154(3)
220	49(2)	47.9(17)	145(3)
210	45(2)	45.7(16)	136(3)
200	43(2)	43.0(15)	130(3)
190	40(2)	39.1(15)	120(3)
180	38(2)	40.2(14)	116(2)
170	35(2)	35.2(14)	105(2)
160	33.8(18)	33.8(12)	101(2)
150	30.4(17)	31.3(12)	92(2)

140	24.7(17)	26.3(12)	76(2)
130	22.7(16)	24.9(12)	70(2)
120	19.6(16)	23.6(12)	63(2)
110	15.0(16)	20.7(11)	51(2)
100	12.9(16)	17.6(11)	43.4(19)
90	8.3(15)	17.7(11)	34.3(18)
80	3.7(15)	19.1(10)	26.5(18)
70	-0.8(15)	18.1(10)	16.6(18)
60	0.0(15)	2.6(10)	2.6(18)
50	−2.1(15)	−2.9(10)	−7.1(18)
40	−4.1(15)	−4.6(10)	−12.9(18)
30	−4.2(14)	−4.3(10)	−12.6(17)
20	−2.7(14)	−2.8(10)	−8.1(17)
10	−0.3(14)	−0.7(10)	−1.3(17)
15	−1.4(13)	−1.7(9)	−4.5(16)
25	−3.5(14)	−4.3(10)	−11.4(17)
35	−4.3(15)	−4.7(10)	−13.3(18)
45	−3.6(14)	−3.5(10)	−10.7(17)
55	−0.4(14)	−3.6(10)	−4.3(18)
65	0.2(15)	8.9(10)	9.2(18)
75	0.1(14)	24.7(10)	25.0(18)
85	7.0(15)	17.3(10)	31.3(18)
95	9.9(15)	18.3(10)	38.1(18)
105	14.4(15)	19.9(11)	48.8(18)
115	17.7(15)	21.6(11)	56.9(19)
125	22.2(16)	24.4(11)	68.8(19)
135	24.1(16)	27.0(12)	75(2)
145	28.2(17)	29.4(12)	86(2)
155	31.1(18)	31.4(12)	94(2)
165	34.1(19)	35.5(13)	104(2)
175	36.0(19)	37.5(13)	110(2)
185	40(2)	39.4(14)	119(2)
195	41(2)	41.5(14)	124(2)
205	45(2)	43.5(14)	133(2)
215	47(2)	46.4(14)	140(3)
225	50(2)	49.7(15)	150(3)
235	52(2)	50.1(16)	155(3)

Section S3. Parameterisation of the volume thermal expansion

A variety of physically meaningful functional forms may be used to fit the temperature variation of lattice parameters as a function of temperature. Following closely the example used in my previous work,[22] the volume thermal expansion is parameterised using a model in which the vibrational density of states (VDOS) is described by two Debye-type functions and an Einstein-type function. A more detailed justification for the application of this model is given in my earlier work.

The temperature dependence of the molar volume is thus described as

$$V = V_0 \left[1 + \frac{f(\theta_{D1})}{X} + \frac{f(\theta_{D2})}{Y} + \frac{f(\theta_E)}{Z} \right] \tag{1}$$

where V_0 is the molar volume at zero temperature, the Debye functions and the Einstein function, $f(\theta_{D1})$, $f(\theta_{D2})$ and $f(\theta_E)$, represent different components of the crystal's internal energy and X, Y and Z are 'mixing parameters'. Where the volume is described in terms of single Debye temperature in a first-order expansion of the internal energy the term X, for example, would be $V_0 K_0 / \gamma$, where V_0 and K_0 are the zero-temperature molar volume and bulk modulus and γ is a Grüneisen parameter. For the three-term model given in Eq. 1 it is sufficient to note that $X \propto \gamma_x^{-1}$, where γ_x is a Grüneisen parameter corresponding to the vibrational modes described by $f(\theta_{D1})$.

The Debye and Einstein functions are defined as

$$f(\theta_D) = 9 N k_B T \left(\frac{T}{\theta_D} \right)^3 \int_0^{\theta_D/T} \frac{x^3}{e^x - 1} dx \tag{2}$$

$$f(\theta_E) = 3 N k_B \left(\frac{\theta_E}{e^{\theta_E/T} - 1} \right) \tag{3}$$

where N is the number of atoms per molecules, k_B is Boltzmann's constant, T = temperature, and θ_D and θ_E are characteristic Debye or Einstein temperatures, respectively, corresponding to the cut-off frequencies of particular vibrational modes in the VDOS.

It was clear by visual inspection that the volume thermal expansion in D_2O ice obtained by slow cooling, and subjected to various thermal protocols, does not differ substantially from that of flash-frozen ice. A fit of the double-Debye + Einstein model using the same cut-off frequencies as were reported previously (Table S3, column 1) produced a satisfactory fit to the Series 1A/1B data with only small adjustments to the mixing parameter values (Table S3, column 2). In fact the difference in the X parameter can be attributed to poor sampling of the lattice-parameter saturation below 10 K in this study. Free refinement of all parameters (Table S3, column 3) yields a small improvement in the quality of the fit.

Table S3: Parameters obtained by fitting of a model constructed from a double-Debye + Einstein-type function (Eqs. 1 – 3).

		Quenched D_2O ice Fortes[22] Series 1 & 2	Naturally-frozen ice This work, Series 1 Frequencies fixed	Naturally-frozen ice This work, Series 1 All parameters free
V_0	$(cm^3\ mol^{-1})$	19.31434 ± 0.00006	19.31418 ± 0.00011	19.31401 ± 0.00022
V_0	$(Å^3)$	128.2889 ± 0.0004	128.2878 ± 0.0007	128.2867 ± 0.00011
θ_{D1}	(K)	88.9 ± 6.6	*88.9*	87.4 ± 9.8
θ_{D2}	(K)	476.9 ± 18.9	*476.9*	477 ± 20
θ_E	(K)	937 ± 43	*937*	938 ± 42
X	$(J\ mol^{-1})$	$-317 \pm 24\ x10^4$	$-299.1 \pm 2.4\ x10^4$	$-307 \pm 30\ x10^4$
Y	$(J\ mol^{-1})$	$48.6 \pm 2.2\ x10^4$	$47.0 \pm 0.2\ x10^4$	$47 \pm 2\ x10^4$
Z	$(J\ mol^{-1})$	$42.2 \pm 1.1\ x10^4$	$47.1 \pm 0.4\ x10^4$	$46 \pm 1\ x10^4$
Residual sum of sq.		$3.167\ x10^{-4}$	$3.277\ x10^{-6}$	$2.714\ x10^{-6}$

A discussion of the physical meaning of these parameters is given by Fortes.[22] The volume thermal expansion calculated from this model fit is shown below with the raw derivatives from the current study of pure ice in Figure S1a, from the previous work in Figure S1b and with this work's KOD-doped ice data in Figure S1c. It is apparent that the scatter in the data from the earlier work is larger (by a factor of ~ 2) than in the current work. The standard deviation of the model residuals are $2.2\ x10^{-6}$ for the three data series measured in 2017 and $9.8\ x10^{-7}$ for the seven data series measured in 2018. This is almost certainly due to the extra care afforded to ensure good thermal equilibration of the sample at each temperature point, equilibration time being increased from 5 minutes to 10 minutes. There is a small but clear deviation from the model fit in the region between 100 and 150 K and above 230 K, which probably reflects the lack of any description in the model of the effect on the VDOS of partial ordering ± any structural relaxation as well as poor sampling of the higher frequency portion of the VDOS.

Figure S1.

(a) Volume thermal expansion data and model fit (solid black line) from the current work. The dashed blue line is taken from the capacitance dilatometry study of single-crystal D_2O ice by Buckingham.[23] The general deviation that grows with temperature may reflect poor thermal equilibrium of the crystal with its surroundings whilst the larger deviation at high temperatures may be due to incomplete correction for the effects of sample sublimation.

(b) Volume thermal expansion data from the previous work[22] compared with the model fit (solid black line) from the current work. **(c)** Volume thermal expansion of KOD-doped D_2O ice Ih compared with the model fit (solid black line) from the analysis of pure D_2O ice.
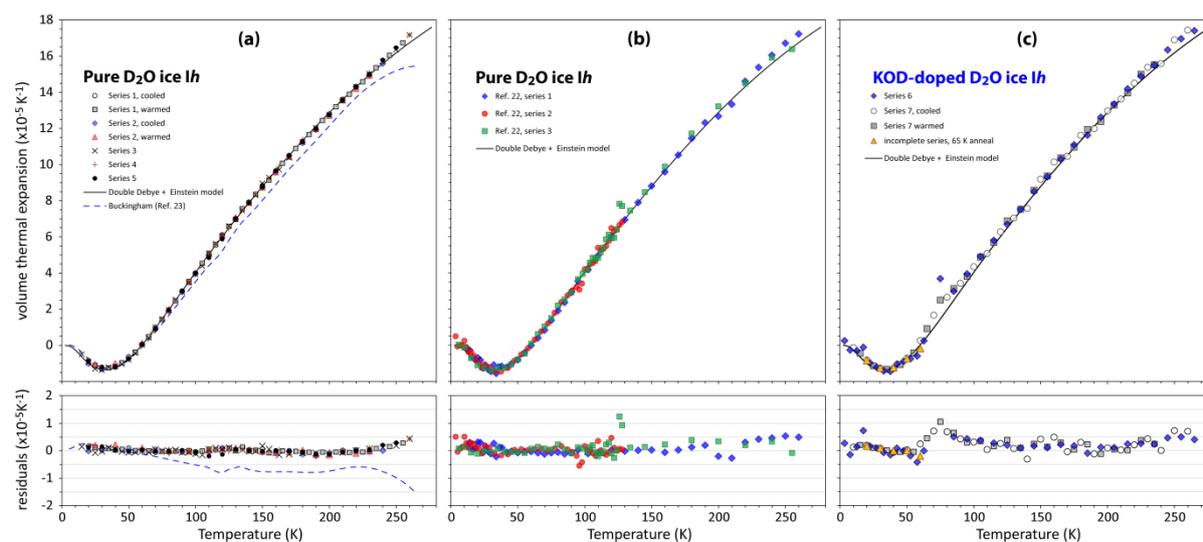
There is little change in the temperature at which the volume thermal expansion turns negative, 59.75 K (59.9 K in the previous work) or the temperature of the negative expansion minimum, 32.0 K (32.6 K previously). Despite small anomalies in α_V between 100 and 150 K, the level of reproducibility of this quantity, across ten different temperature series on six independently-prepared and loaded specimens measured over two years is very good. Clearly, this description of the thermal expansion is sufficiently robust for most ordinary purposes; for example, applications in modelling of icy planetary bodies.

Electronic Supplementary Information

Section S4. Analytical description of the *c/a* ratio temperature dependence

The objective is to present an analytical approximation to the temperature dependence of the *c/a* ratio in ice I*h* and use that to calculate the effect on the *c*-axis linear expansion of freezing-in non-equilibrium values of the axial ratio and allowing that quantity to either merge smoothly with the equilibrium value or to undergo a sharp relaxation. The underlying assumption of this model is that features in *c/a* are <u>entirely</u> due to the behaviour of the *c*-axis. This is, of course, not entirely true since there is a small lattice-parameter dispersion in the *a*-axis at low temperature, but it is approximately three times smaller than the relative dispersion in the *c*-axis length. It is nevertheless self-evident from the calculations below that this simple model gives an accurate representation of the thermal expansion anomalies and aids in understanding their origin where absolute lattice parameters (and thus absolute *c/a* ratios) may be unavailable, such as in dilatometry studies.

The linear expansion of the *c*-axis, $\alpha_c = \frac{1}{c}\frac{dc}{dT}$

where the temperature dependence of the *c*-axis length, $c(T) = a(T) \cdot (c/a)(T)$

The temperature dependence of the *a*-axis length is obtained by approximating a three term Einstein model of the vibrational spectrum to experimental values:

$$a(T) = a_0 + \left[\frac{x}{exp(\theta_{E1}/T) - 1}\right] + \left[\frac{y}{exp(\theta_{E2}/T) - 1}\right] + \left[\frac{z}{exp(\theta_{E3}/T) - 1}\right]$$

These parameters have the following values:

a_0	4.4976				
x	−0.003	y	0.0230	z	0.1746
θ_{E1}	85	θ_{E2}	240	θ_{E3}	600

The temperature dependence of the axial ratio is approximated as:

$$(c/a)(T) = P(T) \cdot m(T) + (1 - P(T)) \cdot n(T) \cdot Q(T)$$

Both *m(T)* and *n(T)* are polynomial curves intended to represent the upper and lower bounds of the axial ratio's temperature dependence, with the smooth variation between them being described primarily by a Gompertz function, *P(T)*, with an additional logistic function, *Q(T)* being employed to describe the shape of the discontinuity in the 100 – 130 K region.

$$m(T) = uT^3 + vT^2 + wT + (c/a)_{high}$$

$$n(T) = uT^3 + vT^2 + wT + (c/a)_{low}$$

$u = 8.2 \times 10^{-12}$, $v = 7.2 \times 10^{-9}$, $w = 3.3 \times 10^{-8}$, $(c/a)_{high} = 1.62865$ and $(c/a)_{low} = 1.62825$.

$$P(T) = a \cdot exp\left(-b \cdot exp(-c(T - T_1))\right)$$

In all of the models described subsequently, except model Type 4, the parameters in this equation take the values, $a = 1.1$, $b = 0.6$, $c = 0.035$ and $T_1 = 145$ K; this is the solid black line in Figure 5 of the main text and supplementary figures S2 – S3, below. N.B., in this case $Q(T) = 1$.

In order to demonstrate the effect of frozen-in c/a ratios and of the structural relaxations in the 100 – 130 K region, I use,

$$Q(T) = \frac{d + (e - d)}{1 + exp\big(f(T - T_2)\big)}$$

The parameters adopted for each of the curves used in various figures, both here and in the main text, are given below.

Model **Type 1**: Frozen-in c/a ratios with no relaxation. The coloured lines referred to are plotted in Figure 5a – 5c of the main text.

	d	e	f	T_2
Solid black line*	-	-	-	-
Dotted blue line	1.00000	1.00005	0.10	115
Dashed green line	1.00000	1.00010	0.07	124
Dashed orange line	1.00000	1.00015	0.06	135
Solid red line	0.99999	1.00025	0.05	170

* $Q(T) = 1$

Model **Type 2**: Frozen-in c/a ratios <u>with</u> relaxation. The coloured lines referred to are plotted in Figure 5d – 5f of the main text.

	d	e	f	T_2
Dotted blue line	1.00000	1.00005	0.35	100
Dashed green line	1.00000	1.00010	0.25	105
Dashed orange line	1.00000	1.00015	0.20	110

Model **Type 3**: (a) Samples with the same degree of frozen-in c/a ratio but with varying degrees of relaxation. The coloured lines referred to are plotted in Supplementary Figure S2 below.

	d	e	f	T_2
Dotted blue line	1.00000	1.00010	0.35	100
Dashed green line	1.00000	1.00010	0.22	106
Dashed orange line	1.00000	1.00010	0.15	112

Model **Type 4**: (a) Hypothetical different variations in the overall temperature dependence of the c/a ratio. In all cases shown here, $Q(T) = 1$. The coloured lines referred to are plotted in Supplementary Figure S3 below.

	a	b	c	T_1
Solid black line	1.10	0.60	0.035	145
Dotted blue line	1.13	0.60	0.025	150
Dashed green line	1.16	0.65	0.018	152
Dashed orange line	1.10	1.00	0.050	133
Solid red line	1.10	1.00	0.080	135

Figure S2
(a) Hypothetical variations of the c/a ratio, following model Type 3; solid black and red lines are as shown in the Type 1 example (Fig. 5). (b) Calculated linear expansion along the c-axis for these scenarios; the feature marked (1) is similar to what was observed in my earlier study of H_2O ice Ih (Ref. 22, Figures 9 and 12). (c) Enlarged view of the region where step-like anomalies in the linear expansion occur.
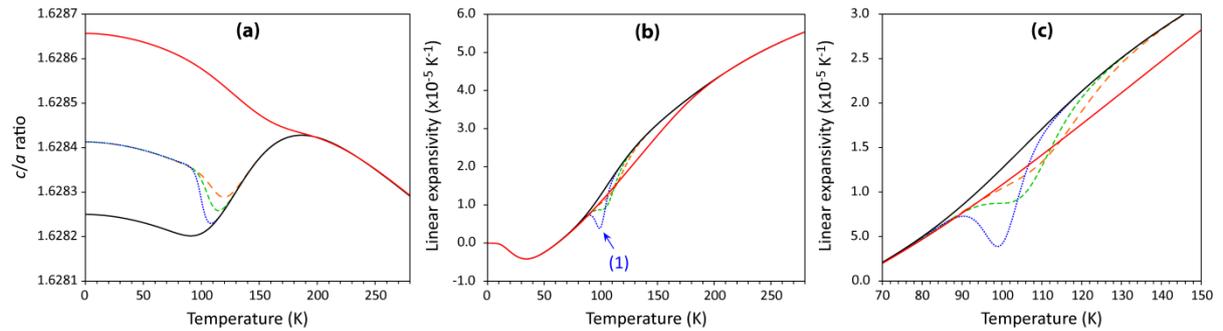
Figure S3
(a) Hypothetical variations of the c/a ratio, following model Type 4. (b) Calculated linear expansion along the c-axis for these scenarios. The very steep turn-over depicted by the red curve, which leads to the sharp rise followed by a plateau in α_c, is a reasonable approximation to the behaviour seen in KOD-doped ice (*cf*., Fig. 4f).
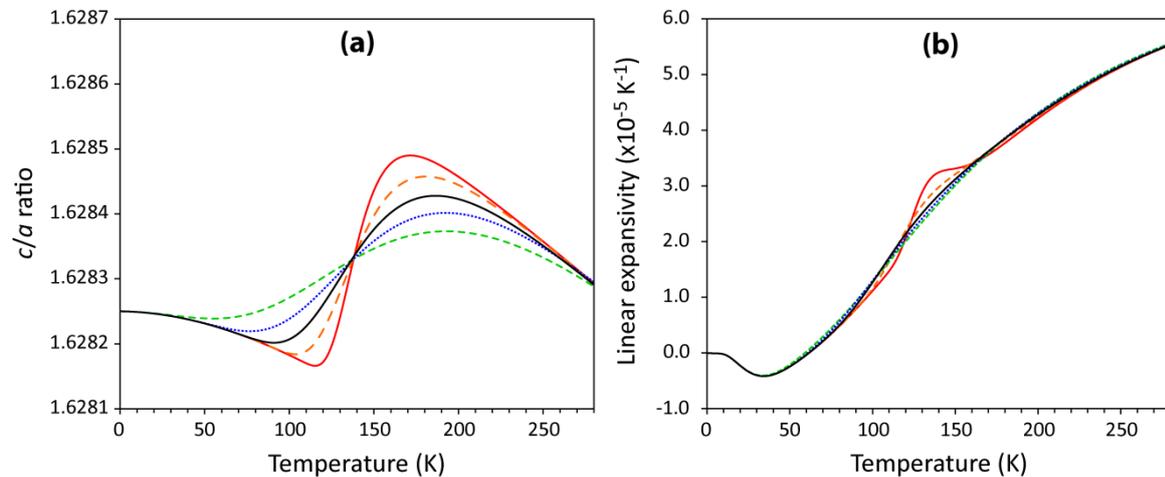
Section S5. Additional supplementary figures

Figure S4

Relaxation times in H_2O and D_2O ice as a function of T.[15,16,23,33,35,36,38-40] The bold dashed red lines bounding the spread of low-T data depict activation energies due to orientational defects ($E_A = 59$ kJ mol^{-1}, $\tau_0 = 1.50 \times 10^{-16}$ s) and ionic defects ($E_A = 20$ kJ mol^{-1}, $\tau_0 = 2.20 \times 10^{-8}$ s). Finer dotted lines show different values of the parameter 'p' (in black) proposed by Popov et al.[44] to characterise the resistance to defect migration from correlated movement of orientational and ionic defects. Higher values of p are indicative of greater influence on the relaxation time from orientational defects. The shaded region shows the range of temperatures over which relaxation times of $10^3 - 10^4$ s may occur in ice by virtue of the sample-specific defect population.
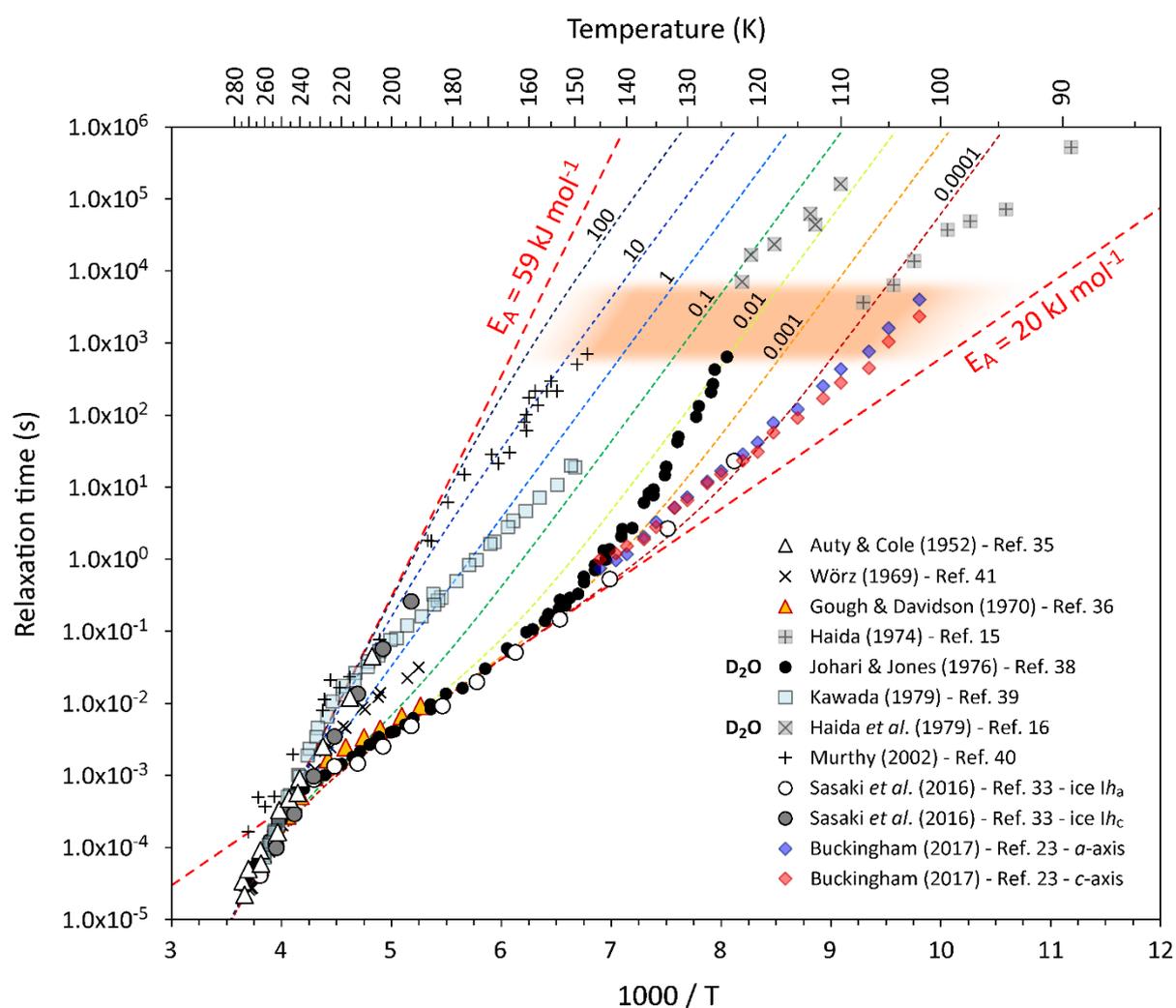
Figure S5

Neutron powder diffraction data measured in HRPD's 90° detector banks for a representative set of data collected at 10 K in the current study. In all cases, the lack of any diffuse scattering between the strong (011), (020) and (100) peaks is evidence, along with the near uniform sharpness of all peaks, that the samples are not significantly affected by stacking faults.
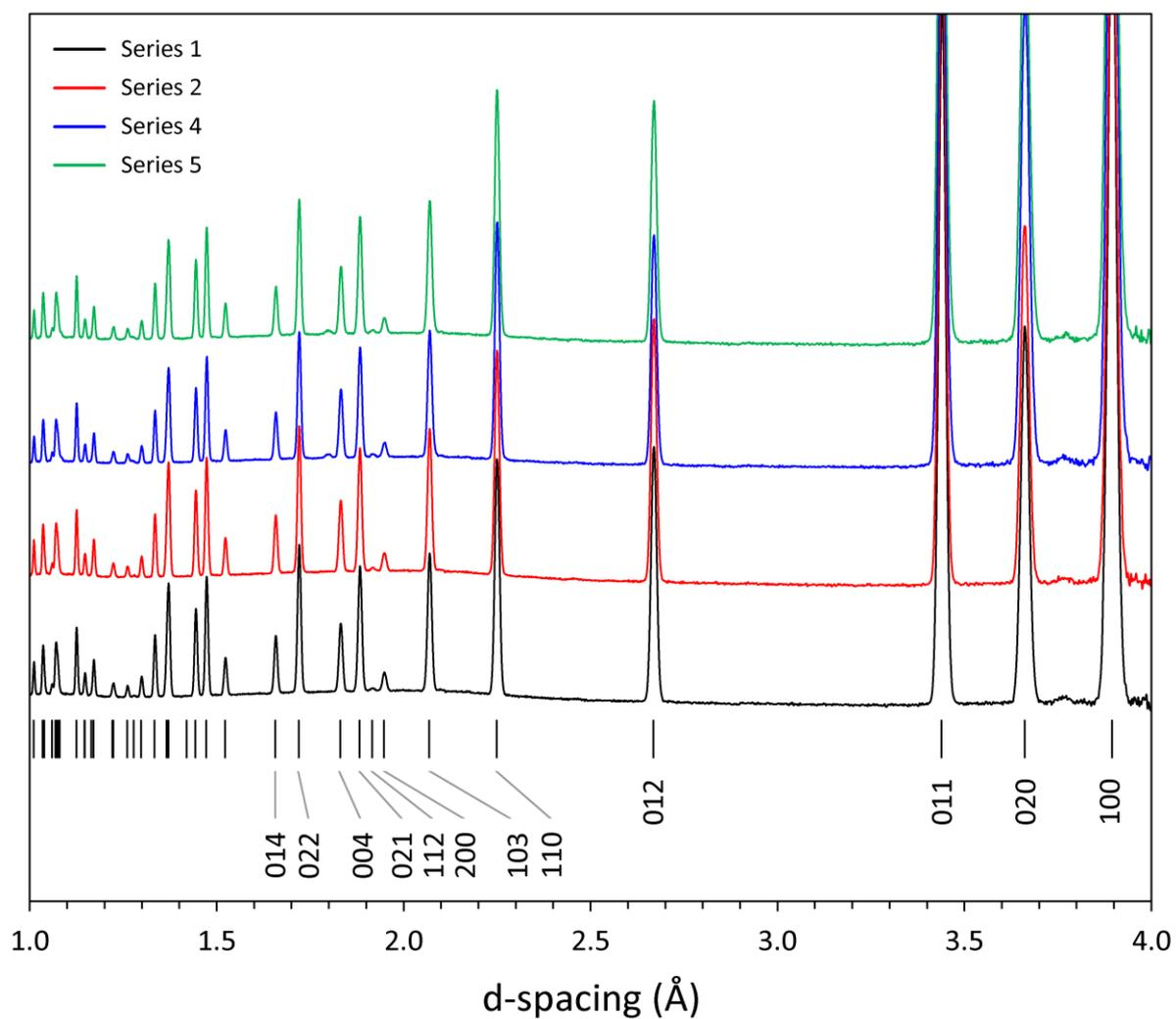
Figure S6

Variation of the full width at half maximum of the (002) and (011) Bragg peaks – measured in HRPD's 90° detector banks – as a function of temperature. **(a)** The naturally-frozen, slow-cool / slow warm observations (Series 1) exhibit no discernible variation in peak width with temperature. By contrast, the flash-frozen samples exhibit broadening of up to 8 % that do vary with temperature. **(b)** It is clearer from the plot of (011) peak widths that the onset of the sharpening in the flash frozen samples occurs at 150 K on warming, with each becoming as sharp or even sharper than the naturally-frozen ice specimens at higher homologous temperatures. It is noteworthy that, despite being synthesised in a similar way to the 2018 quenched pipette droplets, the 2017 quench samples exhibit a much smaller degree of peak broadening. It seems likely that other undocumented (and indeed unmeasurable) aspects of the sample preparation have a significant effect on the diffraction characteristics of the specimen. **(c)** and **(d)** Variation in peak widths obtained in Series 2, where the sample was quenched from 265 to 77 K in 90 seconds and then cooled to 10 K over the course of another hour. The grey background symbols depict the data shown in Figure S6a and S6b. Evidently, the rapid quenching and freezing-in of the high-temperature disorder (and high-temperature c/a ratio) does not result in any broadening due to inhomogeneous strain.
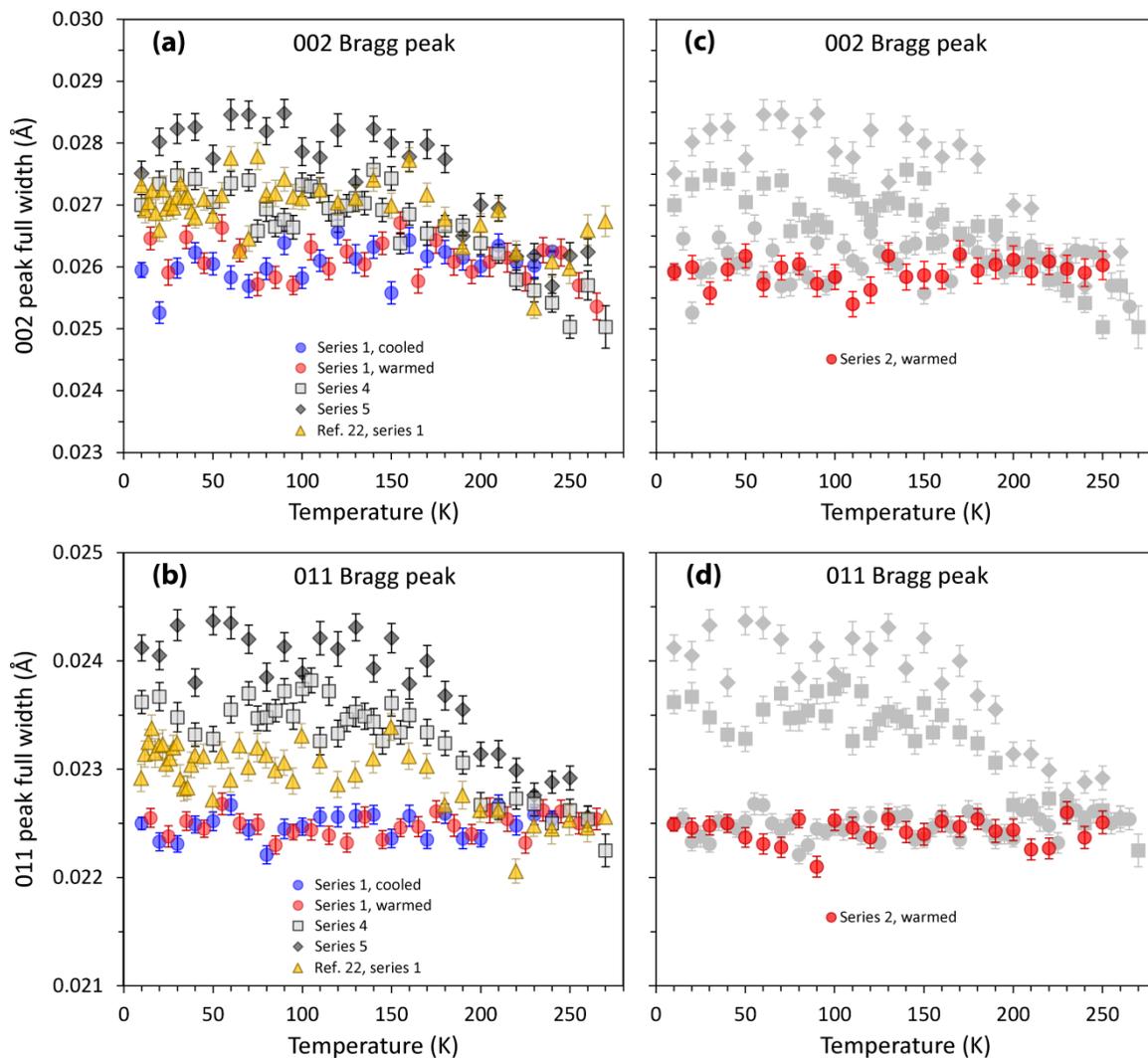
Figure S7.

(a) For context, the widths of the (002) peak shown in Figure S6 are compared with the widths observed in heavily stacking-faulted ice formed by the back-transformation of high-pressure ice VI. **(b)** Neutron powder data measured in HRPD's 90° detectors during the transition from ice VI→ ice Ih via stacking-faulted ice I$_{SD}$, showing the large variations in peak width, intensity and diffuse background that occur during this transformation.
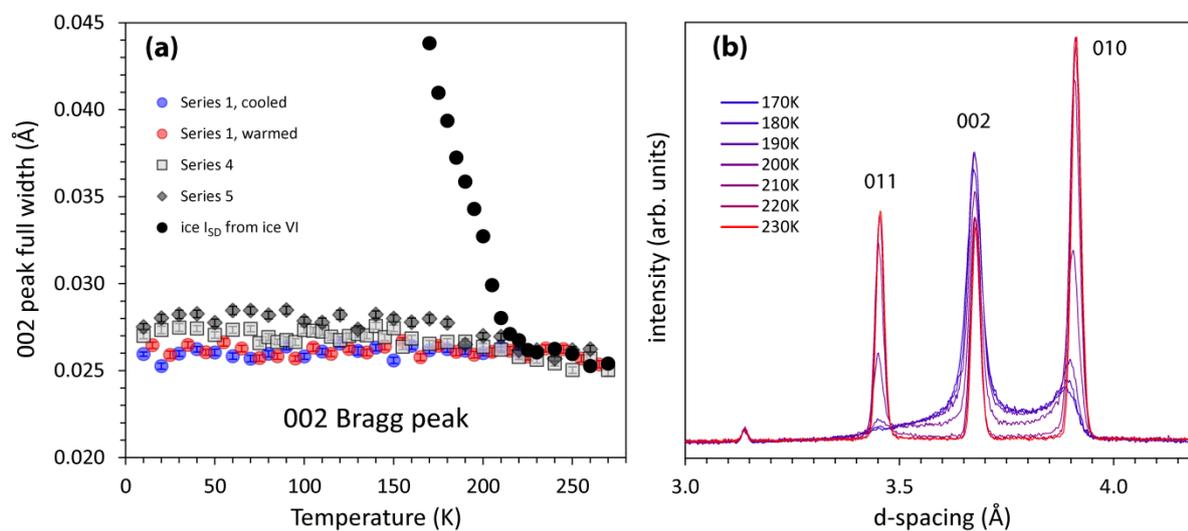
Section S6. References

Literature cited in this Supplement (complete numbered list in main text)

[22] A. D. Fortes, Accurate and precise lattice parameters of H_2O and D_2O ice Ih between 1.6 and 270 K from high-resolution time-of-flight neutron powder diffraction data. *Acta Crystallogr. B* **74**, 196–216 (2018).

[23] D. T. W. Buckingham, High-resolution thermal expansion and dielectric relaxation measurements of H_2O and D_2O ice Ih. PhD Thesis, Montana State University (2017).

[33] K. Sasaki, R. Kita, N. Shinyashiki, S. Yagihara, Dielectric relaxation time of ice-Ih with different preparation. *J. Phys. Chem. B*., **120**, 3950–3953 (2016).

[35] R. P. Auty, R. H. Cole, Dielectric properties of ice and solid D_2O. *J. Chem. Phys*., **20**, 1309–1314 (1952).

[38] S. R. Gough, D. W. Davidson, Dielectric behavior of cubic and hexagonal ices at low temperatures. *J. Chem. Phys*., **52**, 5442–5449 (1970).

[59] G. P. Johari, S. J. Jones, Dielectric properties of polycrystalline D_2O ice Ih (hexagonal). *Proc. R. Soc. London A*, **349**, 467–495 (1976).

[39] S. Kawada, Dielectric properties of heavy ice Ih (D_2O ice). *J. Phys. Soc. Japan*, **47**, 1850–1856 (1979).

[40] S. S. N. Murthy, Slow relaxation in ice and ice clathrates and its connection to the low-temperature phase transition induced by dopants. *Phase Trans*., **75**, 487–506 (2002).

[41] O. Wörz, R. H. Cole, Dielectric properties of ice I. *J. Chem. Phys*., **51**, 1546–1551 (1969).

[44] I. Popov, I. Lunev, A. Khamzin, A. Greenbaum, Y. Gusev, Y. Feldman, The low-temperature dynamic crossover in the dielectric relaxation of ice Ih. *Phys. Chem. Chem. Phys*., **19**, 28610–28620 (2017).